PAPER R

CORE ANALYSIS OF WEST TEXAS SHALLOW-SHELF CARBONATES: RESERVOIR CHARACTERIZATION AND CO_2 MONITORING

Richard C. Nolen-Hoeksema

ABSTRACT

A core analysis program was conducted to provide supporting data to a crosswell demonstration field experiment (DFE) carried out by the Stanford University Seismic Tomography Project. The DFE is being conducted to demonstrate the use of crosswell seismic tomography for reservoir characterization and monitoring the seismic effects of CO_2 flooding. This report examines the core-analysis results to see if it is feasible to identify seismic property changes in response to CO_2 flooding.

The contrast between a CO_2-swept zone and an unswept zone averages a small 2% if one uses P-wave velocities (v^*_p). The contrast is somewhat better for P-wave and bulk-wave impedances, averaging 3% and 4.5%, respectively. The best contrast comes from the bulk moduli (K*) where the estimated contrast averages about 8%.

INTRODUCTION

A pilot project is being conducted in a West Texas carbonate reservoir to evaluate the performance of a hybrid CO_2-injection scheme. The Stanford University Seismic Tomography Project (STP) is a participant in this project through a demonstration field experiment (DFE) to investigate the use of crosswell seismic tomography for (1) reservoir characterization and (2) monitoring CO_2 injection. Stanford University conducted two crosswell seismic surveys in December 1991 between wells A and B and between wells A

and C. We reported these crosswell seismic results last year [STP-3, 1992]. Herein, I report core-analysis results in support of the STP project.

Well A was drilled as an observation well for the CO_2-injection pilot project. The well was drilled to a depth of 3260 feet. A total of 285 feet of 3.25-inch diameter, unoriented core was cut between 2,775 and 3,060 feet. The principal pay interval in well A is the D5 unit of the Grayburg formation and was cored between 2,863 and 2,947 feet. Minor secondary pay zones were also cored above and below the D5 unit, in the E and M Grayburg units, respectively. The top of the San Andres formation was cored at a depth of 3,038 feet.

In this report, I describe the core-analysis programs, ultrasonic velocity data, and methods I used to estimate sonic and seismic properties from core data. I extend the sonic-log matching calculations to estimate the effects of CO_2 flooding on the seismic properties of the Grayburg formation. These estimates suggest that the contrast between a CO_2-swept zone and an unswept zone is a small 2% if one uses P-wave velocities. The contrast is somewhat better for P-wave and bulk-wave impedances, being 3% and 4.5%, respectively. The best contrast comes from the bulk moduli where the estimated contrast is about 8%.

CORE ANALYSIS PROGRAMS

Routine Full-Diameter Core Analysis

Core Laboratories in Midland, Texas, did routine full-diameter core analysis of the core. This consisted of taking 6-inch long full-diameter samples from each foot of core. Core Laboratories cleaned the samples using a low-temperature toluene-CO_2 extraction method. The low temperature (less than 104°F or 40°C) minimized dehydration of the gypsum ($CaSO_4 \cdot 2H_2O$) that is in the rock. Fluid saturations were determined from the fluids collected during core cleaning. After each sample was cleaned and dried, porosity, permeability, and grain density were determined. This first porosity measurement is referred to as the "low temperature porosity".

After these measurements were made, the core samples were heated to drive off the water of hydration in the gypsum. After the samples cooled, a second porosity measurement was made. This second porosity, referred to as the "high temperature porosity", is greater than the low-temperature porosity. Estimates of gypsum content come from the high-temperature porosity, assuming the increase in porosity (i.e., pore volume) results from volume lost by gypsum caused by dehydration.

Routine Core Analysis of Plug Samples

We selected vertical plugs from 16 locations, based on core-to-log gamma-ray correlations, log data (density, neutron, sonic), and hand-specimen examination. We cut mostly vertical plugs to favor the dominant propagation direction of sonic-log signals. We also wanted a few horizontally oriented plugs to capture some aspect of P-wave anisotropy. So at 4 locations we selected horizontal plugs cut from the same stratigraphic horizon as their companion vertical plugs. As we wanted to sample both reservoir and non-reservoir zones, nine plug locations were in reservoir zones and seven locations were in non-reservoir zones. These data appear in Table 1.

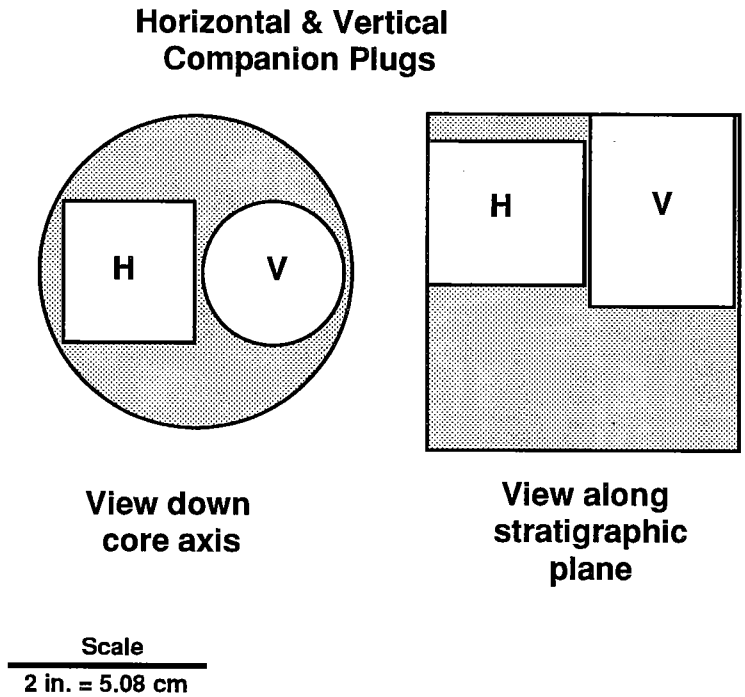

Sketch of how horizontal and vertical companion plugs were cut.

The plugs were 1.5 inches in diameter and 1.5 to 2.0 inches long. The horizontal plugs were shorter than the vertical plugs because of the core's small diameter.

As with the full-diameter samples, Core Laboratories cleaned the plugs using a low-temperature oil extraction method.

After drying the plugs, Core Laboratories determined the porosity, permeability and grain density, all at room temperature and pressure conditions. Bulk volume (V_b) was measured using Archimedes' principle, whereby each sample was immersed to a common depth in mercury. Grain volume (V_g) was measured using a helium pycnometer. Pore

volume (V_p) was calculated $V_p = V_b - V_g$. Porosity (ϕ) was calculated $\phi = V_p/V_b$. The dry weight (W_{dry}) was measured. Assuming dry weight equals the weight of the grains (W_g), grain density (ρ_g) was calculated $\rho_g = W_{dry}/V_g$. Steady-state permeability to air was measured. Dry bulk density (ρ_d) is:

$$\rho_d = \frac{W_{dry}}{V_b} = (1-\phi)\rho_g. \quad (1)$$

Saturated bulk density (ρ^*) is:

$$\rho^* = \rho_d + \phi \cdot \rho_f = \rho_d + \phi \cdot \sum_i S_i \rho_i \quad (2)$$

where ρ_f is the fluid density, S_i is the pore-volume fraction or saturation of the *i*-th fluid component, and ρ_i is the density of the *i*-th fluid component.

These data appear in Table 1. Porosity ranges from 0.3 to 22.1 percent. Steady-state permeability to air ranges from less than 0.01 to 66.7 mD. (Note that Core Laboratories' steady-state permeameter cannot resolve permeabilities below 0.01 mD, so there is an artificial floor of 0.01 mD to the permeability values. Rocks with permeabilities below 0.01 mD are considered effectively impermeable to fluid flow.) Grain density ranges from 2.72 to 2.88 g/cm^3.

Figure 1 is a plot of permeability versus porosity for the 20 plug samples. Figure 2 is a plot of vertical permeability versus porosity from the full-diameter measurements and is shown for comparison with Figure 1. Figure 1 is a very limited data set. It shows a semi-log linear trend. A truer picture is given by Figure 2, which shows a weak trend with tremendous scatter in the data. This scatter reflects the significantly heterogeneous nature of these dolomitic rocks. Plug pairs 6 and 8 are from the Grayburg D5 reservoir zone and illustrate this heterogeneity. The pairs were collected side-by-side within the same stratigraphic horizon, yet their porosities differ significantly within the pair.

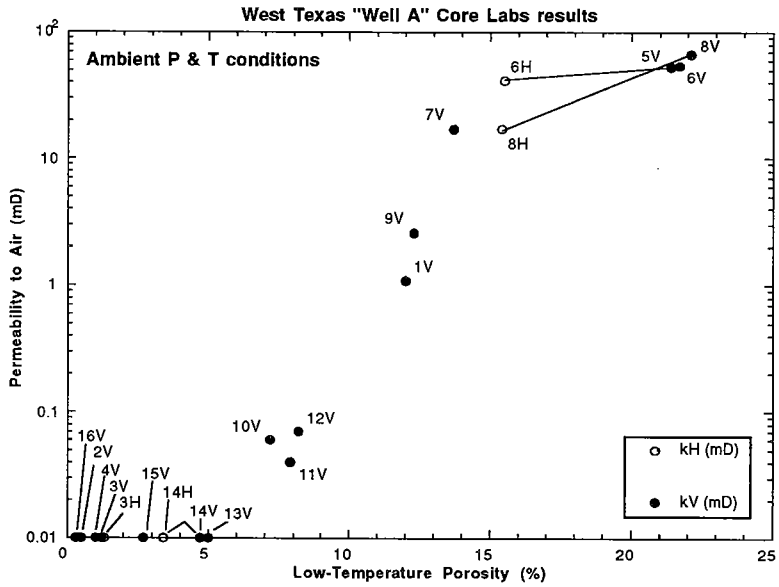

Figure 1

Figure 1: Permeability versus porosity for the 20 plug samples.

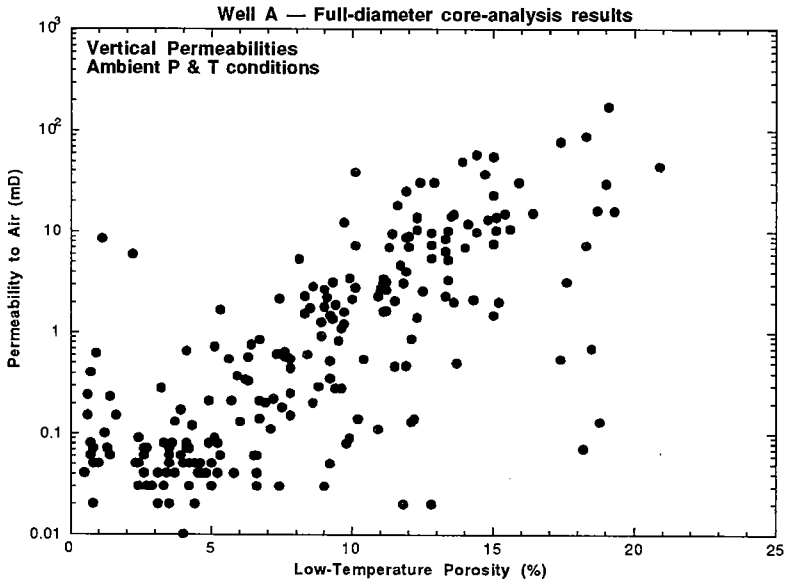

Figure 2

Figure 2: Vertical permeability versus porosity from the full-diameter measurements, shown for comparison with Figure 1.

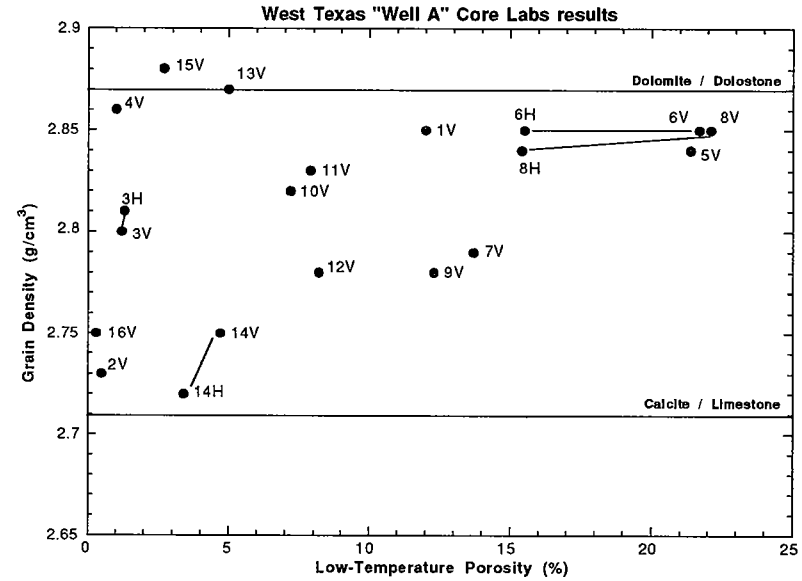

Figure 3

Figure 3: Grain density versus porosity for the 20 plug samples.

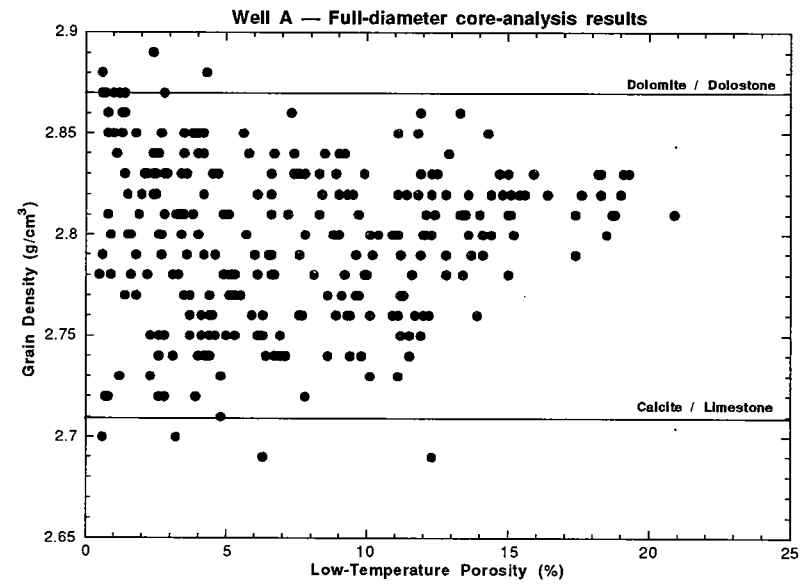

Figure 4

Figure 4: Grain density versus porosity from the full-diameter measurements, shown for comparison with Figure 3. There is no relationship between grain density and porosity.

Figure 3 is a plot of grain density versus porosity for the 20 plug samples. The plug pairs are identified by connecting lines. Figure 4 is a plot of grain density versus porosity from the full-diameter measurements and is shown for comparison with Figure 3. Figure 3 is a very limited data set. Comparison with Figure 4 indicates there is no relationship between grain density and porosity. As expected, grain density and porosity are intrinsic rock properties that are independent of one another.

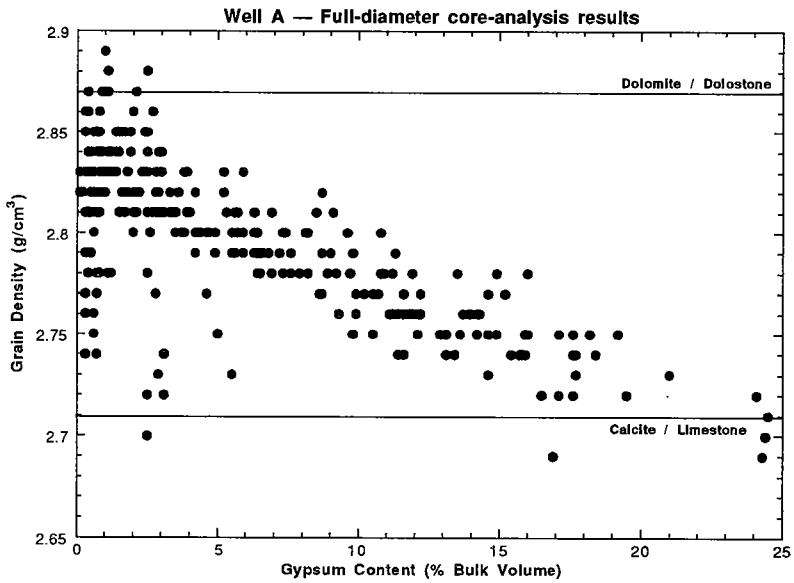

Figure 5

Figure 5: Grain density versus gypsum content from the full-diameter measurements, shown for comparison with Figures 3 and 4. There is a definite decrease in grain density with increasing gypsum content.

Figure 5 is a plot of grain density versus gypsum content from the full-diameter measurements and is shown for comparison with Figures 3 and 4. The grain densities for pure calcite and dolomite are indicated for comparison. As expected, there is a definite relation of decreasing grain density with increasing gypsum content. Grayburg formation deposition occurred as shallow-shelf carbonate muds [Ward et al., 1986], primarily limestone, which has a grain density of 2.71 g/cm^3. After deposition, secondary dolomitization converted the rocks to dolostone, which has a grain density of 2.87 g/cm^3. Following dolomitization the rocks were commonly cemented with anhydrite (ρ_g = 2.96 g/cm^3) and gypsum (ρ_g = 2.31 g/cm^3). If the primary cement was anhydrite, then an increase in the grain-volume fraction of anhydrite would cause the overall grain density to increase above 2.87 g/cm^3. On the other hand, if the primary cement was gypsum, then an

increase in the grain-volume fraction of gypsum would cause the overall grain density to decrease below 2.87 g/cm^3. Figure 5 shows a definite decrease in grain density with increasing gypsum content. Gypsum appears to be the primary cement in these rocks.

Ultrasonic Measurement Program

The 20 plugs were sent to Verde GeoScience for ultrasonic velocity measurements, after completion of the measurements by Core Laboratories. Compressional (P) and two independent, orthogonally polarized shear (S1, S2) velocities were measured. As the plugs and the core were not oriented, no attempt was made to align the shear polarizations to any planar features in the core. Shear velocities reported here are averages of S1 and S2. The central frequency for the P and S ultrasonic transducers was 1 MHz. The plugs were measured dry (pores filled with air) and fully saturated with oil-field brine. The dry and saturated measurements were made at 4 differential pressures ($P_{diff} = P_{confining} - P_{pore}$): 1000, 2000, 3000, and 5000 psid. For the dry measurements the pore pressure was 0 psig and for the saturated measurements the pore pressure was 1000 psig. Resolution of the first-break picks was ±0.01 μsec. Precision of the P and S velocities was conservatively ±0.5%.

Compressional velocity (v_p), shear velocity (v_{s1}, v_{s2}, avg. v_s), v_p/v_s ratio, dynamic bulk modulus (K), dynamic shear moduli (G), and dynamic Young's modulus (E) were tabulated in the Verde GeoScience report. I have plotted all the data for each plug sample in Appendix A.

Ultrasonic Velocities

In this paper, I concentrate on the velocity measurements made at a differential pressure of 2000 psid (13.8 MPa). The West Texas reservoir is at a depth of about 3000 feet. The lithostatic stress gradient in the area is about 1 psi/ft and the reservoir pressure is about 1000 psig. Therefore, it is most appropriate to examine the velocities in this data set that were measured at 2000 psid. Table 2 lists these data.

Figures 6 and 7 are graphs of velocity versus porosity for the P-wave and S-wave velocities, respectively. In each figure, the open circles are the dry data and the filled circles are the saturated data. The dashed and solid best-fit lines are for dry and saturated data, respectively. The best-fit lines show that the velocities clearly decrease with increasing porosity.

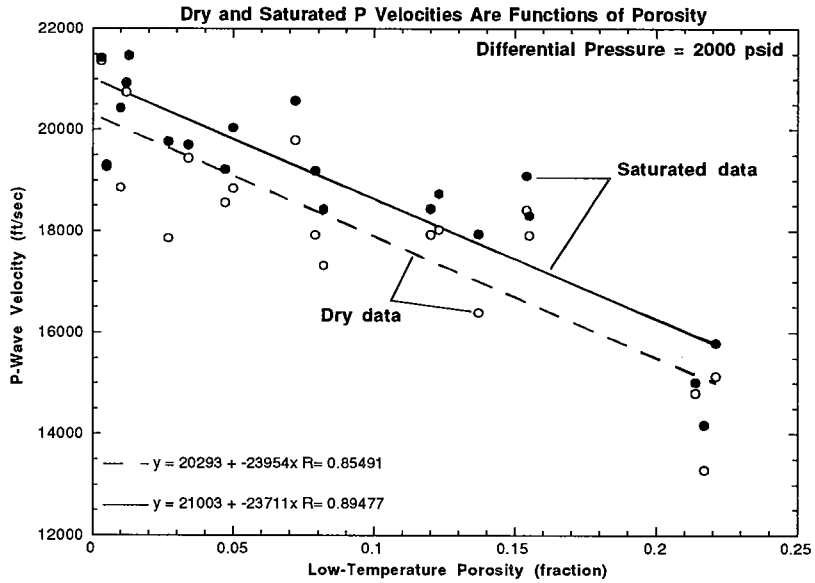

Figure 6

Figure 6: P-wave velocity versus porosity.

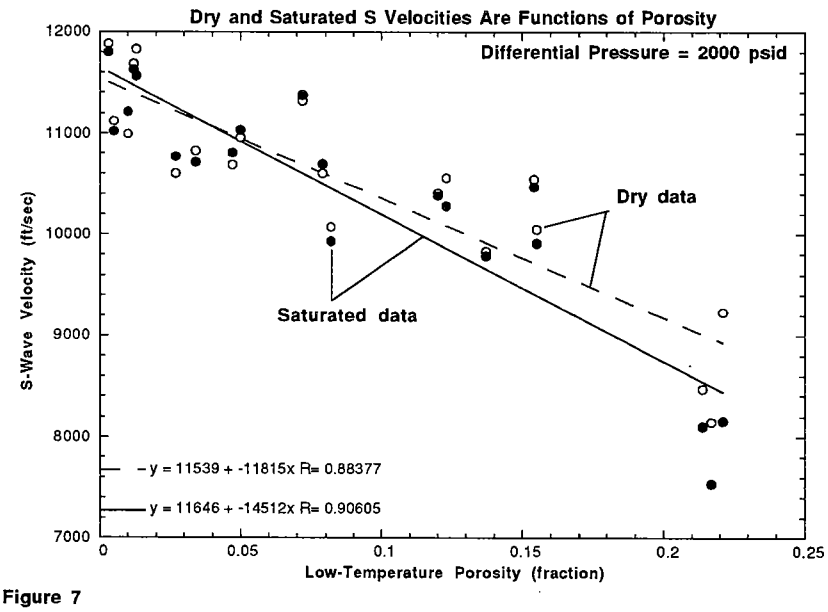

Figure 7

Figure 7: S-wave velocity versus porosity.

Figure 8 is a graph of $\Delta v = (v_{sat}-v_{dry})/v_{dry}$ versus porosity for both P and S velocities. It shows the effect of 100% replacement of air by oil-field brine. There is an average 4.2% increase in P-wave velocity and an average 1.5% decrease in S-wave velocity, when the rocks are saturated with brine as compared to when the rocks are dry (Table 2).

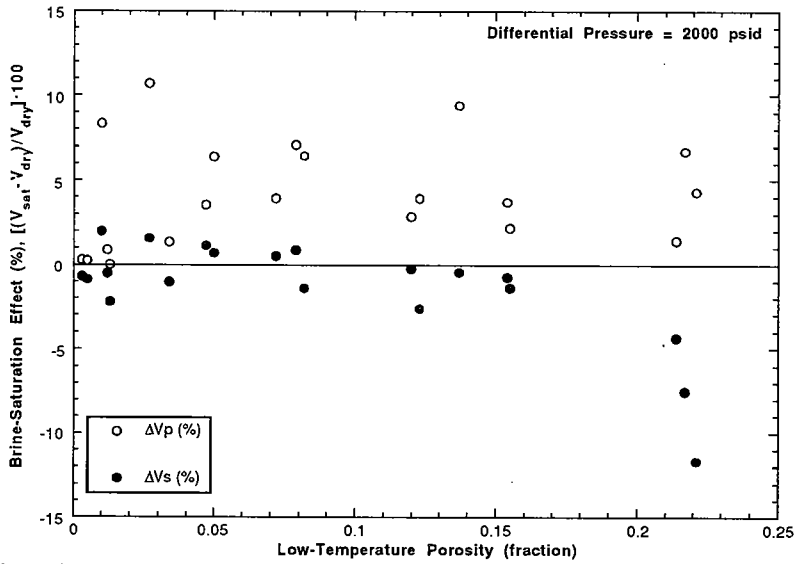

Figure 8: $\Delta v = (v_{sat}-v_{dry})/v_{dry}$ versus porosity for both P and S velocities, showing the effect of 100% replacement of air by oil-field brine.

The saturated P-wave velocity

$$v^*_p = \sqrt{\frac{K^*+(4/3)G^*}{\rho^*}} \qquad (3a)$$

is affected by brine saturation through the saturated-rock bulk modulus (K*) and bulk density (ρ*). At a constant saturation, the effect of brine saturation on P waves ($|\Delta v|_p$) is highest in low-porosity rocks because the density effect is smallest and the effect of pore-fluid substitution on pore stiffness is largest. As porosity increases, the density effect increases and the bulk-modulus effect decreases.

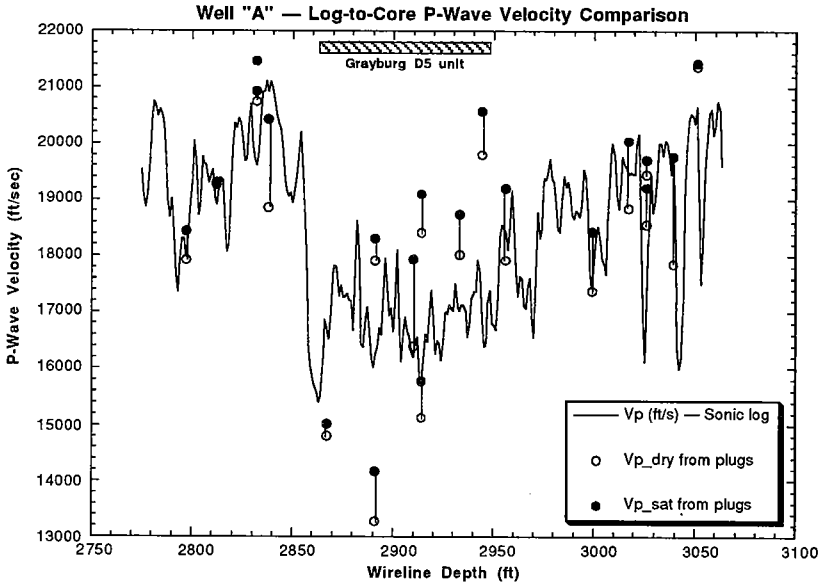

Figure 9

Figure 9: Comparison of ultrasonic core and sonic-log P-wave velocities.

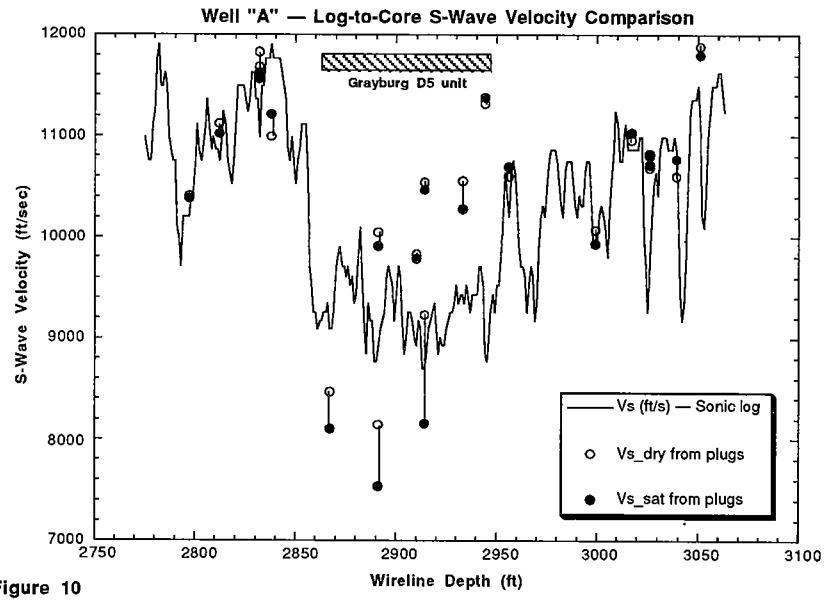

Figure 10

Figure 10: Comparison of ultrasonic core and sonic-log S-wave velocities.

For saturated S-wave velocities,

$$v^*_s = \sqrt{\frac{G^*}{\rho^*}} \ , \tag{3b}$$

replacement of air by brine does not affect the shear modulus (G*) but causes the saturated bulk density (ρ*) to increase. The density effect gets larger as porosity increases, which causes v^*_s to decrease and the magnitude of the brine effect on S waves ($|\Delta v|_s$) to increase (Figure 8).

Figures 9 and 10 compare the ultrasonic core velocities to the sonic-log velocities for P and S waves, respectively. For the most part, ultrasonic velocities are higher than sonic-log velocities. There is more mismatch in the data within the main reservoir zone between 2860 and 2950 feet than there is above and below this zone. The two data sets generally follow each other and correlate with a linear coefficient of best-fit (r^2) of about 0.5. Some mismatch is expected. The two measurements sampled different paths, path lengths, and scales of heterogeneities. Using a velocity range of 10,000–20,000 ft/sec (3,048–6,096 m/sec), the ultrasonic transducers have a resonant frequency of 1 MHz and produce signals with 0.12–0.24 in. (0.3–0.6 cm) wavelengths. These are "point" measurements over path lengths of 8–16 wavelengths (i.e., 2-inch long plugs), affected by inch-scale heterogeneities (e.g., plug pairs 6H & 6V and 8H & 8V). In contrast, sonic logs have resonant frequencies about 15–20 kHz and produce signals with 0.5–1.3 ft (15–40 cm) wavelengths. Using a velocity range of 10,000–20,000 ft/sec (3,048–6,096 m/sec), they measure path lengths of 8 feet or more (8–16 wavelengths) and are affected by heterogeneities of several inches to feet. The mismatch between the ultrasonic and well-log velocities is attributable, in part, to these factors.

SEISMIC AND SONIC VELOCITIES

Ultrasonic P-wave velocities are affected by fluid effects because of scattering, solid-fluid inertial effects, and grain-scale local flow effects [e.g., Mavko and Jizba, 1991]. Velocities in saturated rock measured at ultrasonic frequencies are often faster than velocities measured at lower seismic and sonic frequencies. Velocities in dry rock are largely insensitive to the frequency of measurement. Gassmann's [1951] equation relates the saturated-rock bulk modulus (K*) to the dry-rock bulk modulus (K_d). It applies at low frequencies where scattering, solid-fluid inertial effects, and grain-scale local flow effects are negligible. Seismic and sonic frequencies typically lie within this low-frequency band.

Therefore, my approach has been to use the dry ultrasonic data and Gassmann's equation to estimate the effects of fluid saturation on measurements at seismic and sonic frequencies.

Gassmann's [1951] equations are low-frequency (i.e., zero-frequency) estimates of the fluid-saturated moduli, when the dry-frame moduli, mineral moduli, fluid moduli, and porosity are known. The saturated bulk modulus (K*) is given by

$$K^* = K_d + K_p = K_d + \frac{\left(1 - \frac{K_d}{K_m}\right)^2}{\frac{\phi}{K_f} + \frac{1-\phi}{K_m} - \frac{K_d}{K_m^2}} \tag{4a}$$

where K_d is the dry-frame bulk modulus, K_m is the mineral bulk modulus, K_f is the fluid modulus, K_p is the bulk modulus of the fluid-filled pore space, and ϕ is porosity. The shear modulus is assumed to be unaffected by saturation, so

$$G^* = G_d \tag{4b}$$

where G* is the saturated-rock shear modulus and G_d is the dry-frame shear modulus.

Estimation of Sonic Velocities from Core Measurements

To estimate the sonic-log velocities, I wanted to take advantage of the full-diameter core samples. These samples were selected every foot of the core. I used the following basic procedure:

1) Estimate the mineral moduli (K_m & G_m) from the grain-density measurements on the plug samples (Appendix B).
2) From measurements of dry-rock ultrasonic velocities, density and porosity on the plug samples, obtain linear least-squares regression fits to dry-rock moduli (K_d & G_d) versus porosity (ϕ). These fits have the form: $K_d/K_m = f(\phi)$ and $G_d/G_m = f(\phi)$.
3) Estimate the mineral moduli (K_m & G_m) from the grain-density measurements on the full-diameter core samples (Appendix B).
4) Apply the $K_d/K_m = f(\phi)$ and $G_d/G_m = f(\phi)$ linear-regression fits obtained in Step 2 to the full-diameter-core estimates of mineral moduli to obtain estimates of the dry-rock moduli (K_d & G_d) for each foot of core.

5) Use Gassmann's equations 4a and 4b to obtain estimates of the low-frequency, saturated-rock moduli (K* & G*) for each foot of core.
6) Calculate saturated-rock densities (ρ*) using equations 1 and 2.
7) Calculate the saturated-rock velocities (v^*_p & v^*_s) using equations 3a and 3b.

For brine, I used density $\rho_f = 1.028$ g/cm^3 based on measurements of the reservoir brine, bulk modulus $K_f = 2.5$ GPa, and velocity = 5116 ft/sec (1560 m/sec) [Long and Chierici, 1961; Carmichael, 1989, p. 469].

I explored three methods to estimate the grain moduli, K_m and G_m, from the grain-density information. I call these three methods the dolomite-calcite transform, the dolostone-limestone transform, and the core-constrained transform. Details about these transforms are given in Appendix B. In this section, I only discuss the results and how they compare to the open-hole sonic logs from Well A.

Using the dolomite-calcite transform, I assumed the principal mineral components of the Grayburg formation were calcite and dolomite. Assuming a two-phase system, the transform estimates the mineral modulus M_m using

$$M_m = M_1 + \int_0^{X_2} \frac{\partial M_m}{\partial X_2} dx_2' = M_1 + \frac{\partial M_m}{\partial X_2} X_2 \quad ; \quad X_1 + X_2 = 1, \tag{5a}$$

where M_m is the desired estimate of the effective mineral modulus (K_m or G_m), X_1 and X_2 are the grain-volume fractions of pure end-member phases 1 and 2, and M_1 and M_2 are mineral moduli of phase 1 and 2. X_1 and X_2 vary from 0 to 1. The quantity $\partial M_m/\partial X_2$ is presumed constant and equal to $(M_2–M_1)$. One can think of equation 5a as being the grain-density weighted arithmetic average between the mineral moduli M_1 and M_2 of the pure end-member phases 1 and 2

$$\begin{aligned} M_m &= M_1 + w(M_2 - M_1) \quad ; \quad 0 \le w \le 1 \\ &= M_1 + \frac{(\rho_g - \rho_1)}{(\rho_2 - \rho_1)}(M_2 - M_1) \end{aligned} \quad , \tag{5b}$$

where w is the weighting factor and is equal to X_2, ρ_1 and ρ_2 are the grain densities of the pure end-member phases 1 and 2, and ρ_g is the measured grain density. Here, the grain-density weighting factor (w) is the mineral fraction of dolomite (phase 2). When compared to the sonic logs, this method resulted in saturated velocities that were too high (Figure 11). This dolomite-calcite transform method does not take into account the lower mineral moduli

of the other mineral components in the Grayburg formation, that is, anhydrite, gypsum and quartz [Ward et al., 1986].

Using the dolostone-limestone transform, I assumed the principal rock components of the Grayburg formation were limestone and dolostone. I used equation 5 again, except that now phase 1 was limestone and phase 2 was dolostone. This technique gave a good fit to the sonic logs (Figure 12). In this dolostone-limestone approach the mineral moduli were generally lower than those for dolomite-calcite approach. These lowered moduli capture some of the effects of the other mineral components in the Grayburg formation.

I tried a third method to estimate K_m and G_m, the core-constrained method (Appendix B). I used the full-diameter core measurements to try to estimate the grain-volume fractions of dolomite, calcite, anhydrite, gypsum, and quartz silt. This core-constrained method produced a good fit to the P-wave sonic log (Figure 13), but the fit to the S-wave log was less satisfactory than the when using the dolostone-limestone method (cf. Figure 12). The core-constrained method produces a better fit to the well logs than the dolomite-calcite method (compare Figures 11 & 13). The core-constrained transform method suffered because I did not have reliable quantitative estimates of the mineral fractions in these rocks. The best way to estimate mineral moduli is to use quantitative mineralogy obtained from petrographic and geochemical analyses (e.g., mineral modal analyses).

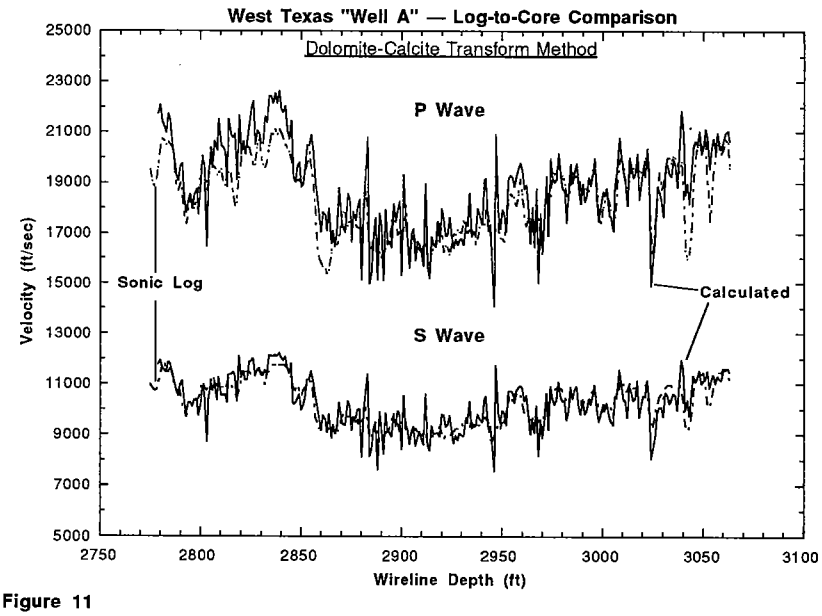

Figure 11: Log-to-core comparison of sonic velocities. Core velocities were calculated using mineral moduli estimated by the dolomite-calcite transform method.

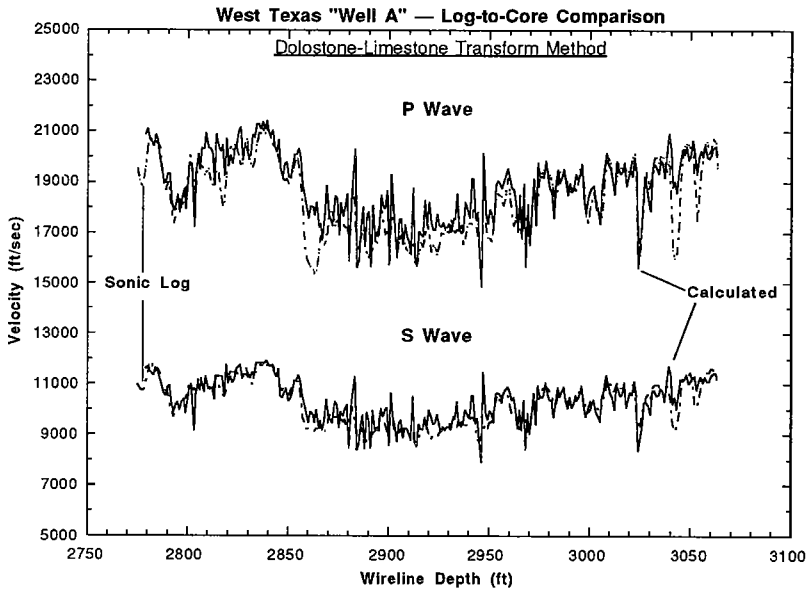

Figure 12: Log-to-core comparison of sonic velocities. Core velocities were calculated using mineral moduli estimated by the dolostone-limestone transform method.

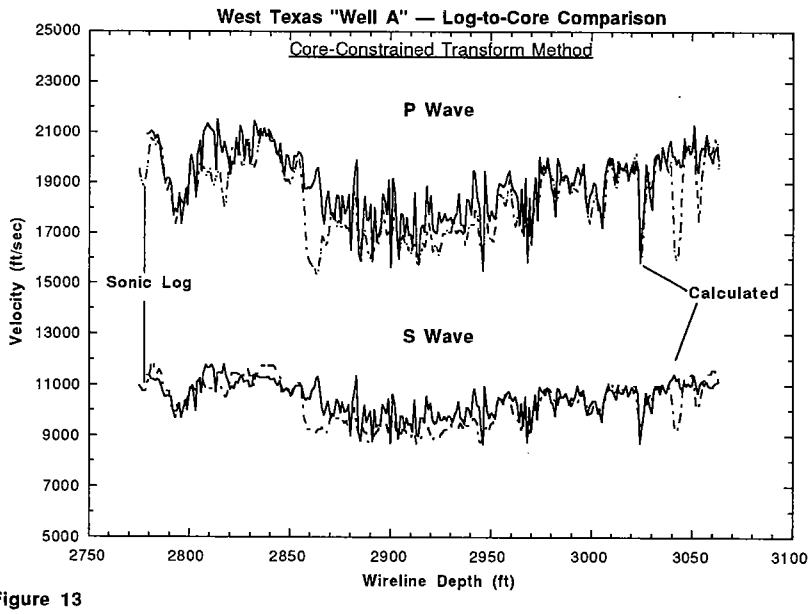

Figure 13: Log-to-core comparison of sonic velocities. Core velocities were calculated using mineral moduli estimated by the core-constrained transform method.

I use the dolostone-limestone method in the rest of this report. It is easy to use, it appears to capture the overall characteristics of the mineralogy, and the resulting fit to both P- and S-wave sonic logs is good (correlation coefficient, r = +0.84; coefficient of determination, $r^2 = 0.71$).

THE BRINE EFFECT — 100% REPLACEMENT OF AIR BY BRINE IN THE PORE SPACE

Table 2 shows that 100% replacement of air by brine in the plug samples produced a measured average v_p increase of 4.18% (range = 0 to 10.71%) and an average v_s decrease of -1.45% (range = -11.68 to +1.98%). For these measured data, there is a very weak (r = 0.13, $r^2 = 0.02$) positive correlation between Δv_p and ϕ and a strong (r = -0.71, $r^2 = 0.51$) negative correlation between Δv_s and ϕ.

I used Gassmann's [1951] equation to estimate the low-frequency "brine effect" (i.e., 100% replacement of air by brine in the pore space). Table 4 shows that the Gassmann equation predicts an average v_p increase of 1.98% (range = -1.13 to 7.48%) and an average v_s decrease of -1.81% (range = -0.05 to -4.75%). There is a weak (r = -0.48, $r^2 = 0.23$) negative correlation between Δv_p and ϕ and a very strong (r = -0.99, $r^2 = 0.99$) negative correlation between Δv_s and ϕ. These negative correlations between Δv and porosity result from the increase in rock density when brine replaces air in the pore space (equations 3a & 3b).

Figure 14 is a comparison of P-wave velocities in brine-saturated and air-saturated (i.e., dry) rocks. This plot was generated using the dry moduli (K_d and G_d) obtained to match the sonic logs (Figure 12). Both air- and brine-saturated v_p's were calculated using these moduli. The lines in Figure 14 were drawn to help visualize the magnitude of the brine effect; the 1:1 line indicates when $v^*_p = v_{pdry}$ and the other lines indicate when v^*_p is 2.5% and 5% greater than v_{pdry}. On average, the brine-saturated velocities are 1.4% higher than the air-saturated velocities (range = 0.03 to 4.9%). The curvature in the data reflects the sensitivity of v_p to changes in fluid content at low porosities (high v_p) and the decreased sensitivity of v_p at high porosities (lower v_p) that results from the opposing density effect (cf. equation 3a). This v_p* versus v_{pdry} relation can be approximated by the exponential relation:

$$v^*_p\,(\mathrm{ft/s}) = 5920\exp\left(6.22\times10^{-5}v_{pdry}\right)$$
$$v^*_p\,(\mathrm{km/s}) = 1.80\exp\left(0.204v_{pdry}\right) \quad \ldots\ r^2 = 0.994.$$

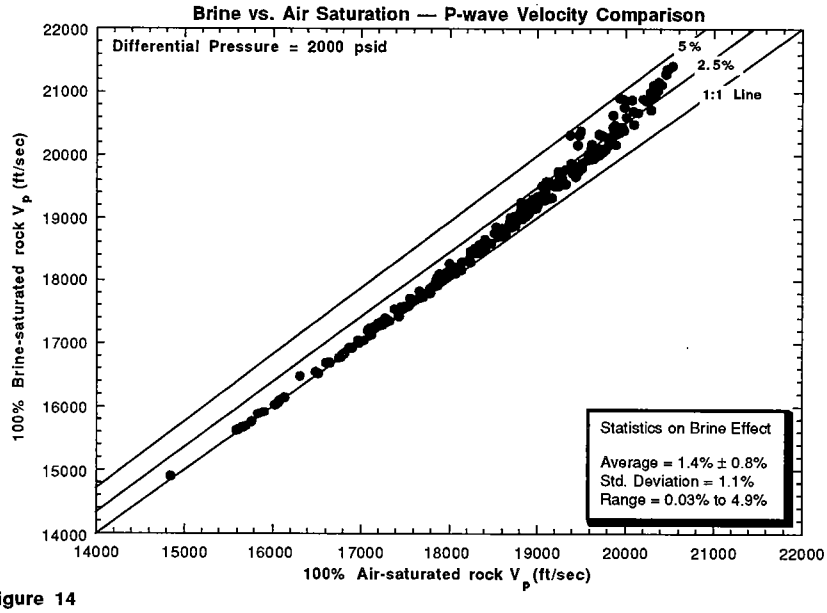

Figure 14

Figure 14: Comparison of P-wave velocities in brine-saturated versus air-saturated rocks. This plot was generated using the dry moduli (K_d and G_d) obtained to match the sonic logs in Figure 12.

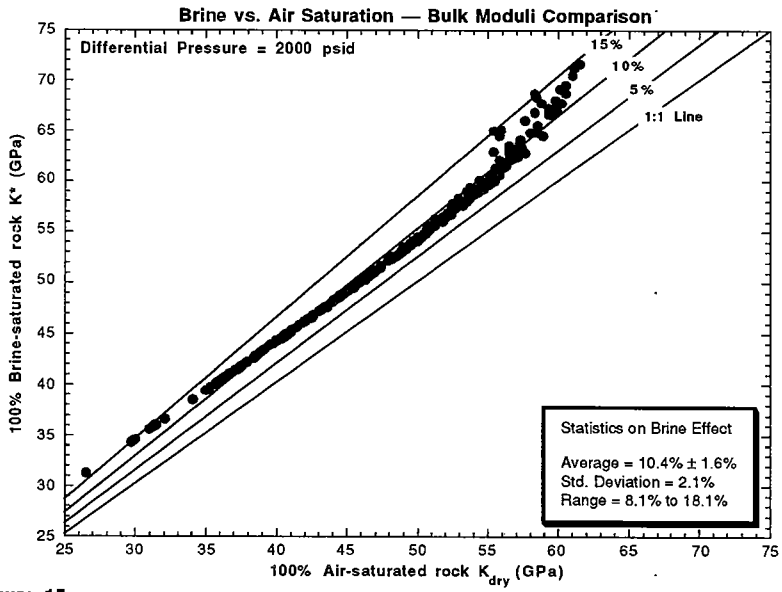

Figure 15

Figure 15: Comparison of saturated versus dry bulk moduli, K* versus K_d. This plot was generated using the dry bulk modulus (K_d) obtained to match the sonic logs in Figure 12.

Another way to look at these data is to compare the saturated versus dry bulk moduli, K* versus K_d (Figure 15). Here the effect of changes in fluid content is quite clear. On average, K* is 10.4% higher than K_d—the average deviation is 10.4 ± 1.6% and the brine effect ranges from 8.1 to 18.1%. The curvature in these data reflects the interaction between the strongest effect of decreasing sensitivity of K* (or $K_p = K^* - K_d$; equation 6a) to changes in fluid content (K_f) with increasing porosity, the intermediate effect of increasing sensitivity of K* with decreasing K_d (i.e., K_d/K_m), and the small effect of increasing sensitivity of K* with increasing K_m. This K* versus K_d relation can be approximated by the exponential relation:

$$K^*(\text{GPa}) = 18.4\exp\left(2.17\times10^{-2}K_d\right) \ldots r^2 = 0.994.$$

As suggested by the average brine effects in Figures 14 and 15, the bulk moduli are more sensitive to changes in fluid content than P-wave velocities. This suggests that to detect the effects of fluid substitution we should be monitoring changes in moduli rather than changes in velocity (e.g., CO_2 flooding of a previously waterflooded reservoir).

Comparisons between Mineral Moduli Estimation Methods

These estimates of the brine effect will depend on the mineral moduli (equation 4a). For example had I used higher mineral moduli, such as those from the dolomite-calcite transform method, these estimates of the effect of brine would have been larger. The tables below give summary statistics of the brine effect for the three methods used to estimate the mineral moduli (Appendix B).

Summary Statistics on Effect of 100% Replacement of Air by Brine on P-wave Velocities
Comparison by mineral moduli estimation method

	Dolomite-Calcite	Dolostone-Limestone	Core Constrained
Average	3.2 ± 1.1%	1.4 ± 0.8%	2.0 ± 0.9%
Std. Deviation	± 1.4%	± 1.1%	± 1.2%
Range	1.1% to 8.5%	0.03% to 4.9%	0.4% to 5.7%

Summary Statistics on Effect of 100% Replacement of Air by Brine on Bulk Moduli
Comparison by mineral moduli estimation method

	Dolomite-Calcite	Dolostone-Limestone	Core Constrained
Average	17.3 ± 2.7%	10.4 ± 1.6%	12.8 ± 2.2%
Std. Deviation	± 3.7%	± 2.1%	± 2.9%
Range	12.2% to 30.8%	8.1% to 18.1%	9.4% to 25.5%

In these tables, the brine effects are expressed using

$$\Delta v_p(\%) = \left(\frac{v^*_p - v_{pdry}}{v_{pdry}} \right) \cdot 100 \qquad \text{and} \qquad \Delta K(\%) = \left(\frac{K^* - K_d}{K_d} \right) \cdot 100$$

for P-wave velocities and bulk moduli, respectively. The dolomite-calcite transform method resulted in the largest estimates of the brine effect. The dolostone-limestone transform resulted in the smallest estimates. The core-constrained method yielded intermediate estimates, which overlapped some with the dolostone-limestone estimates. I believe the most appropriate estimates of the brine effect are those represented by the dolostone-limestone and core-constrained transforms. I use the dolostone-limestone transform here.

ESTIMATES OF CO_2 EFFECTS ON SEISMIC VELOCITIES

The operating temperature in the West Texas reservoir is close to 88°F (31°C). Reservoir fluid pressures range from about 900 psig (6.2 MPa) to about 1200 psig (8.3 MPa) [pers. comm., Paul Griffith, Company reservoir engineer, 1992]. So, I estimated the fluid properties at these reservoir conditions.

The oil in the reservoir is a light oil with API gravity = 30–32° API (≈0.87 g/cm^3). At 88°F, the measured isothermal compressibilities (β_T) of the oil is 5.00×10^{-6} psi^{-1} (0.73 GPa^{-1}) at 900 psig and 4.85×10^{-6} psi^{-1} (0.70 GPa^{-1}) at 1200 psig [pers. comm., Paul Griffith, 1992]. The corresponding isothermal bulk moduli ($K_T = 1/\beta_T$) are 1.38 GPa at 900 psig and 1.42 GPa at 1200 psig. The associated viscosities for this oil are 2.47 cP at 900 psig and 2.50 cP at 1200 psig [pers. comm., Paul Griffith, 1992]. I estimate the P-wave velocity for this oil (v_{poil}) to be 1395 m/sec (4577 ft/sec) at 900 psig and 1405 m/sec (4610 ft/sec) at 1200 psig [Wang, 1988]. Using oil density $\rho_{oil} = 0.87$ g/cm^3, I estimated the corresponding adiabatic (isentropic) bulk moduli ($K_S = \rho_{oil} \cdot v_{poil}^2$) to be 1.69 GPa at

900 psig and 1.72 GPa at 1200 psig. These reservoir oil properties are summarized in the table below.

Oil Properties Used to Estimate Effects of CO_2

T (°F)	P (psig)	K_T (GPa)	Viscosity (cP)	v_{poil} (m/s)	K_{Soil} (GPa)
88	900	1.38	2.47	1395	1.69
88	1200	1.42	2.50	1405	1.72

The reservoir temperature of 88°F (31°C) is right at the critical temperature for pure CO_2. This is the temperature above which pure CO_2 is always in a vapor phase. The reservoir pressures of 900–1200 psig (6.2–8.3 MPa) span across the critical pressure for pure CO_2, which is 1070 psia (7.4 MPa). For West Texas reservoirs, the critical pressure is a good estimate of the minimum miscibility pressure (MMP), above which CO_2 can effectively extract hydrocarbons from crude oil to produce CO_2-hydrocarbon mixtures that are miscible with the oil [pers. comm., F. M. Orr, 1992; Orr and Taber, 1984].

Properties of CO_2 Used in CO_2 Effect Calculations

T (°F)	P (psig)	ρ_{CO2} (g/cm^3)	v_{pCO2} (m/s)	K_{SCO2} (GPa)
88	900	0.19	210	0.008
88	1200	0.70	190	0.025

I used the analytical equation of state given by Bender [1970; pers. comm., Maurice Stadler, Stanford University, 1992] to estimate the density of pure CO_2 . I used the data tabulated by Hilsenrath et al. [1955, 1960] and Vargaftik [1975] to estimate the P-wave velocities of pure CO_2.

To estimate the effects of CO_2 flooding on seismic velocities, I assumed a pre-CO_2, waterflooded reservoir with a water-to-oil ratio of 53% to 47% [pers. comm., Paul Griffith and Brett Newton, Company reservoir engineers, 1992]. After CO_2 has swept through a zone, I assumed a water-oil-gas mixture of 16%–8%–76%. I used the arithmetic average of these fluid components to calculate the densities of these fluid mixtures (ρ_f):

$$\rho_f = \sum_i S_i \rho_i \qquad (6)$$

where S_i is the pore-volume fraction or saturation of the *i*-th fluid component, and ρ_i is the density of the *i*-th fluid component. I used Wood's [1930] isopressure relation for fluid mixtures to calculate the bulk moduli of the fluid mixtures (K_f):

$$K_f = \left[\sum_i \frac{S_i}{K_i} \right]^{-1} \tag{7}$$

where again S_i is the pore-volume fraction or saturation of the *i*-th fluid component, and K_i is the bulk modulus of the *i*-th fluid component. Wood's relation applies when (1) the pressure within each fluid component is the same, (2) the fluid mixture is a multi-component fluid such as gas bubbles in brine or a mixture of oil and brine, and (3) there has been no dissolution of one component in another such as gas dissolved in oil. The properties of these fluid mixtures are given below:

Properties of Fluid Mixtures Used in CO_2 Effect Calculations

T, P	Fluid Property	pre-CO_2 injection (53% oil, 47% brine)	post-CO_2 injection (16% oil, 8% water, 76% CO_2)
88°F, 900 psig	ρ_f	0.94 g/cc	0.37 g/cc
	K_f	1.99 GPa	0.011 GPa
88°F, 1200 psig	ρ_f	0.94 g/cc	0.75 g/cc
	K_f	2.02 GPa	0.033 GPa

These fluid properties were substituted into equations 2, 3 and 4 to estimate the seismic rock properties of pre-CO_2 and post-CO_2 injection conditions. The contrast between these conditions is summarized in the tables below and is shown in Figures 16–19.

Summary Statistics on Effect of CO_2 Injection on P-wave Velocities

Comparison by reservoir conditions

	88 °F, 900 psig	88 °F, 1200 psig
Average	-1.5 ± 0.5%	-2.1 ± 0.3%
Std. Deviation	± 0.7%	± 0.5%
Range	-0.7% to -4.2%	-1.5% to -4.2%

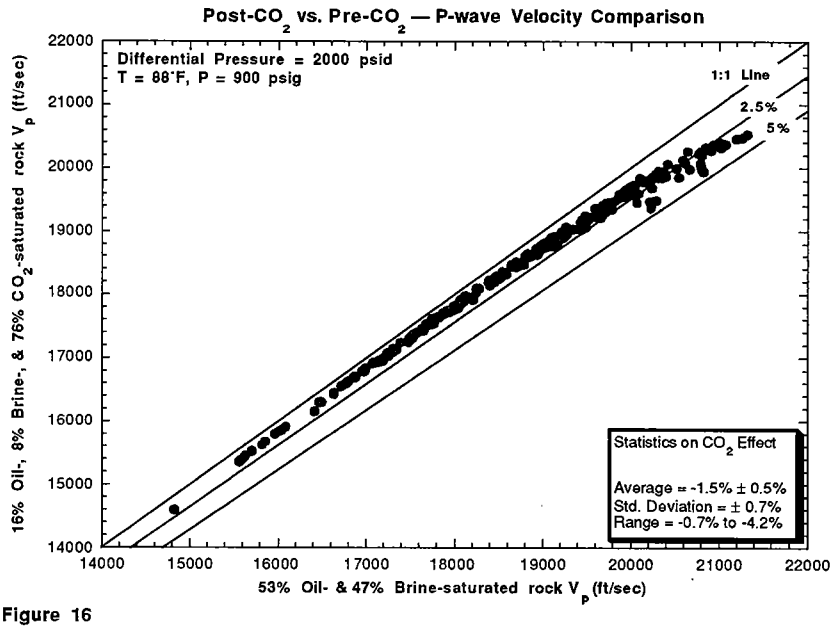

Figure 16

Figure 16: Comparison of P-wave velocities under post-CO_2 versus pre-CO_2 conditions at T = 88°F and P = 900 psig. K_d and G_d were obtained to match the sonic logs in Figure 12.

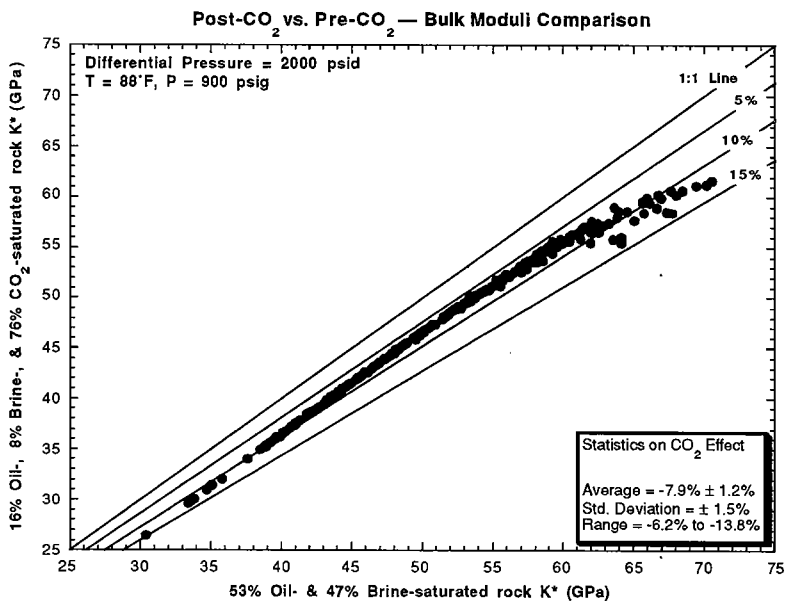

Figure 17

Figure 17: Comparison of bulk moduli under post-CO_2 versus pre-CO_2 conditions at T = 88°F and P = 900 psig. K_d was obtained to match the sonic logs in Figure 12.

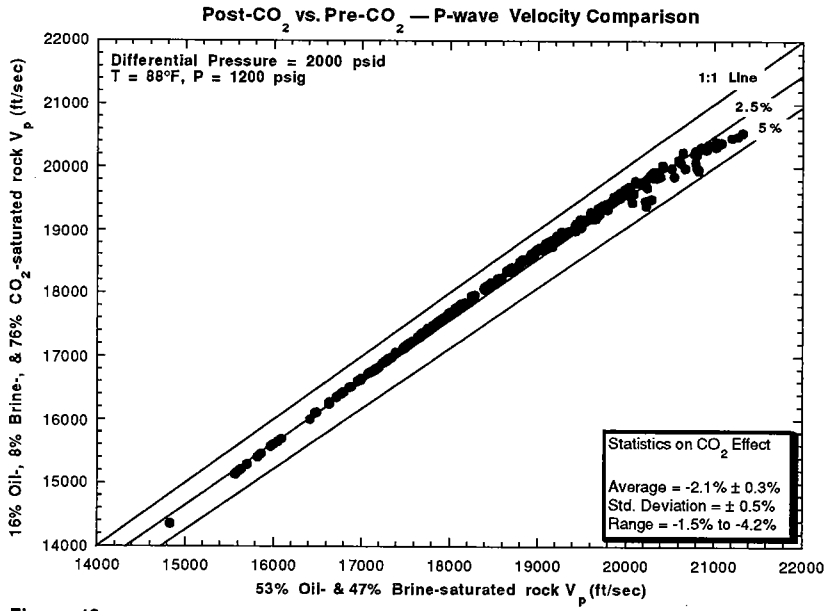

Figure 18

Figure 18: Comparison of P-wave velocities under post-CO_2 versus pre-CO_2 conditions at T = 88°F and P = 1200 psig. K_d and G_d were obtained to match the sonic logs in Figure 12.

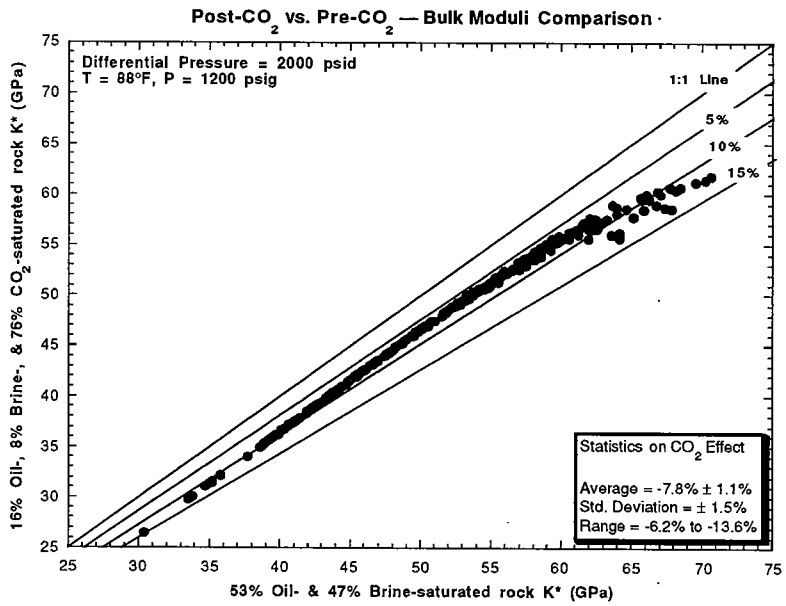

Figure 19

Figure 19: Comparison of bulk moduli under post-CO_2 versus pre-CO_2 conditions at T = 88°F and P = 1200 psig. K_d was obtained to match the sonic logs in Figure 12.

Summary Statistics on Effect of CO_2 Injection on Bulk Moduli
Comparison by reservoir conditions

	88 °F, 900 psig	88 °F, 1200 psig
Average	-7.9 ± 1.2%	-7.8 ± 1.1%
Std. Deviation	± 1.5%	± 1.5%
Range	-6.2% to -13.8%	-6.2% to -13.6%

The contrasts are expressed using

$$\Delta v^*_p\,(\%) = \left(\frac{v^*_{post-CO2} - v^*_{pre-CO2}}{v^*_{pre-CO2}} \right) \cdot 100$$

$$\Delta K^*(\%) = \left(\frac{K^*_{post-CO2} - K^*_{pre-CO2}}{K^*_{pre-CO2}} \right) \cdot 100$$

for P-wave velocities and bulk moduli, respectively. The estimated contrast between pre- and post-CO_2 conditions is a small -2% for P-wave velocities and a larger -8% for bulk moduli. These results emphasize the suggestion that to detect the effects of fluid displacement efforts might be made to monitor changes in moduli rather than changes in velocity (e.g., CO_2 flooding of a previously waterflooded reservoir).

For completeness, let's look at the effect of CO_2 on the P-wave impedance (Z^*_p)

$$Z^*_p = \rho^* v^*_p = \sqrt{\rho^* \left[K^* + (4/3) G^* \right]}. \qquad (8)$$

The table below gives the estimated contrast between pre- and post-CO_2 conditions. The -3% contrast is better than for P-wave velocities but less than for bulk moduli.

Summary Statistics on Effect of CO_2 Injection on P-wave Impedance
Comparison by reservoir conditions

	88 °F, 900 psig	88 °F, 1200 psig
Average	-3.2 ± 0.6%	-2.6 ± 0.4%
Std. Deviation	± 0.8%	± 0.5%
Range	-2.2% to -6.4%	-1.9% to -4.8%

The bulk-wave (K-wave) impedance (Z^*_k)

$$Z^*_p = \rho^* v^*_k = \sqrt{\rho^* K^*} \qquad (9)$$

is more sensitive than Z^*_p but to estimate it requires information on S-wave properties. The table below gives the estimated contrast between pre- and post-CO_2 conditions as being about -4.5%.

Summary Statistics on Effect of CO_2 Injection on Bulk-wave (K-wave) Impedance
Comparison by reservoir conditions

	88 °F, 900 psig	88 °F, 1200 psig
Average	-4.8 ± 0.8%	-4.2 ± 0.7%
Std. Deviation	± 1.0%	± 0.8%
Range	-3.6% to -8.9%	-3.3% to -7.3%

CONCLUSIONS

The P-wave velocity contrast between a CO_2 swept zone and an unswept zone is likely to be small, about a 2% contrast. In comparison, the bulk-modulus contrast is about 4 times larger, about a 8% contrast. This suggests that if we want to monitor CO_2 flooding effects using seismic data we should consider monitoring bulk-modulus changes rather than P-wave velocity changes.

Monitoring P-wave impedance contrasts would be somewhat better than monitoring P-wave velocity contrasts, because the inverse effects of bulk modulus and density for velocity (cf. equation 3) become multiplicative for impedance (cf. equation 8). The K-wave impedance (equation 9) provides a somewhat better impedance contrast.

In order of decreasing sensitivity to changes in fluid content, the seismic properties are:

$$K^* \geq Z^*_k \geq Z^*_p \geq v^*_p.$$

The two most sensitive properties (K^* and Z^*_k) require obtaining S-wave information along with P-wave data, in order for them to be evaluated. However, this should not present an insurmountable problem for crosswell seismic data acquisition. Crosswell P-wave and S-wave data have already be obtained in this West Texas field [e.g., STP-3, 1992].

In this report, I have assumed that the fluids exist as distinct phases and do not dissolve in or become miscible with one another. The reservoir oil is a live oil, i.e., it contains gas

in solution. So the seismic properties of this oil and the unswept zone will be lower than estimated here. During CO_2 flooding under minimum miscibility pressure (MMP) conditions, CO_2-hydrocarbon mixtures become miscible with the crude oil. So the seismic properties of the CO_2-swept zones will be lower than estimated here. Generally, however, I would expect the contrast between a CO_2-swept and an unswept zone to be about the same magnitude as estimated here. More complex calculations could be carried out to provide more accurate estimates of the seismic contrast, provided the fluid phase-behavior data are available.

ACKNOWLEDGMENTS

We thank Chevron Oil Field Research Company (now Chevron Petroleum Technology Company) for providing the field site and co-sponsoring this study with Stanford University. We thank Verde GeoScience, Inc., and Core Laboratories, Inc., for conducting the core measurements. We also thank the Gas Research Institute and the Packard Foundation for their continuing support of the Seismic Tomography Project (STP) at Stanford University.

REFERENCES

Bender, E., 1970, "Equations of state exactly representing the phase behavior of pure substances," Proceedings of the Fifth Symposium on Thermophysical Properties, American Society of Mechanical Engineers, pp. 227–235.

Carmichael, R. S., 1989, "CRC Practical Handbook of Physical Properties of Rocks and Minerals," CRC Press, Inc.

Gassmann, F., 1951, "Über die elastizität poröser medien," Vierteljahrsschrift der Naturforschenden Gesellschaft in Zürich, v. 96, pp. 1–23.

Hilsenrath, J., et al., 1955, 1960, "Tables of thermal properties of gases," Circular 564, National Bureau of Standards, Washington, D.C.

Hill, R. W., 1952, "The elastic behavior of a crystalline aggregate," Proc. Phys. Soc. London, Series A, v. 65, pp. 349–354.

Long, G., and G. Chierici, 1961, "Salt content changes compressibility of reservoir brines," Petroleum Engineering, (July 1961), pp. B25–B31.

Mavko, G., and D. Jizba, 1991, "Estimating grain-scale fluid effects on velocity dispersion in rocks," Geophysics, v. 56, no. 12, pp. 1940–1949.

Orr, F. M., Jr., and J. J. Taber, 1984, "Use of carbon dioxide in enhanced oil recovery," Science, v. 224, no. 4649, pp. 563–569.

STP-3, 1992, Seismic Tomography Project, Volume 3, No. 1, July 1992.

Vargaftik, N. B., 1975, "Tables on the thermophysical properties of liquids and gases," Hemisphere Publishing Co., Washington, D.C.

Wang, Zhijing, 1988, "Wave velocities in hydrocarbons and hydrocarbon saturated rocks—With applications to EOR monitoring," Ph.D. Dissertation, Geophysics Department, Stanford University.

Ward, R. F., C. G. St. C. Kendall, and P. M. Harris, 1986, "Upper Permian (Guadalupian) facies and their association with hydrocarbons—Permian Basin, west Texas and New Mexico," American Association of Petroleum Geologists Bulletin, v. 70, no. 3, pp. 239–262.

Wood, A. D., 1930, "A textbook of sound," G. Bell and Sons, London.

Table 1
Results from Core Laboratories
West Texas "Well A"

Sample Number	Approximate Wireline Log Depth (feet)	Core-Gamma Log Depth (feet)	Reservoir (R) or Non-Reservoir (NR) Rock	Stratigraphic Interval	Permeability		Low-Temperature Porosity (fraction)	Grain Density (g/cc)
					Horizontal (mD)	Vertical (mD)		
1V	2,797.0	2,794.1	R	E to D5		1.08	0.120	2.85
2V	2,810.5	2,807.1	NR	E to D5		<0.01	0.005	2.73
3H	2,831.0	2,826.5	NR	E to D5	<0.01		0.013	2.81
3V	2,831.0	2,826.5	NR	E to D5		<0.01	0.012	2.80
4V	2,837.0	2,833.1	NR	E to D5		<0.01	0.010	2.86
5V	2,868.0	2,865.1	R	D5 to M		53.10	0.214	2.84
6H	2,890.0	2,887.1	R	D5 to M	41.10		0.155	2.85
6V	2,890.0	2,887.1	R	D5 to M		53.90	0.217	2.85
7V	2,910.0	2,907.9	R	D5 to M		16.90	0.137	2.79
8H	2,914.0	2,911.8	R	D5 to M	17.00		0.154	2.84
8V	2,914.0	2,911.8	R	D5 to M		66.70	0.221	2.85
9V	2,933.0	2,928.9	R	D5 to M		2.56	0.123	2.78
10V	2,944.0	2,940.1	R	D5 to M		0.06	0.072	2.82
11V	2,956.0	2,951.9	NR	M to S.		0.04	0.079	2.83
12V	2,999.0	2,997.1	R	M to S.		0.07	0.082	2.78
13V	3,016.0	3,013.9	NR	M to S.		0.01	0.050	2.87
14H	3,026.0	3,024.1	R	M to S.	<0.01		0.034	2.72
14V	3,026.0	3,024.1	R	M to S.		<0.01	0.047	2.75
15V	3,038.5	3,034.5	NR	M to S.		<0.01	0.027	2.88
16V	3,048.5	3,044.5	NR	San Andres		<0.01	0.003	2.75

Table 2
Ultrasonic Velocities Measured at 2000 psid Differential Pressure
West Texas "Well A"

Sample No.	Approx. Wireline Depth (feet)	Res. (R) or Non-Res. (NR)	Stratigraphic Interval	Porosity (fraction)	Perm. (mD)	Grain Density (g/cc)	Dry Measurements		Brine-Saturated Measurements		Measured Brine Effect	
							Vp (ft/s)	Vs (ft/s)	Vp (ft/s)	Vs (ft/s)	ΔVp	ΔVs
1V	2,797.0	R	E to D5	0.120	1.08	2.85	17926	10407	18436	10382	2.85%	-0.24%
2V	2,810.5	NR	E to D5	0.005	0.01	2.73	19263	11117	19309	11019	0.24%	-0.88%
3H	2,831.0	NR	E to D5	0.013	0.01	2.81	21466	11823	21466	11563	0.00%	-2.20%
3V	2,831.0	NR	E to D5	0.012	0.01	2.80	20744	11683	20929	11625	0.89%	-0.50%
4V	2,837.0	NR	E to D5	0.010	0.01	2.86	18853	10992	20428	11210	8.35%	1.98%
5V	2,868.0	R	D5 to M	0.214	53.10	2.84	14809	8471	15022	8103	1.44%	-4.34%
6H	2,890.0	R	D5 to M	0.155	41.10	2.85	17914	10049	18305	9910	2.18%	-1.38%
6V	2,890.0	R	D5 to M	0.217	53.90	2.85	13289	8146	14179	7535	6.70%	-7.50%
7V	2,910.0	R	D5 to M	0.137	16.90	2.79	16397	9830	17944	9786	9.43%	-0.45%
8H	2,914.0	R	D5 to M	0.154	17.00	2.84	18414	10546	19094	10467	3.69%	-0.75%
8V	2,914.0	R	D5 to M	0.221	66.70	2.85	15136	9231	15785	8153	4.29%	-11.68%
9V	2,933.0	R	D5 to M	0.123	2.56	2.78	18027	10556	18735	10280	3.93%	-2.61%
10V	2,944.0	R	D5 to M	0.072	0.06	2.82	19794	11320	20569	11379	3.92%	0.52%
11V	2,956.0	NR	M to S.A.	0.079	0.04	2.83	17923	10603	19193	10695	7.09%	0.87%
12V	2,999.0	R	M to S.A.	0.082	0.07	2.78	17319	10073	18431	9932	6.42%	-1.40%
13V	3,016.0	NR	M to S.A.	0.050	0.01	2.87	18842	10957	20042	11033	6.37%	0.69%
14H	3,026.0	R	M to S.A.	0.034	0.01	2.72	19444	10828	19705	10716	1.34%	-1.03%
14V	3,026.0	R	M to S.A.	0.047	0.01	2.75	18558	10686	19213	10807	3.53%	1.13%
15V	3,038.5	NR	M to S.A.	0.027	0.01	2.88	17856	10602	19769	10768	10.71%	1.57%
16V	3,048.5	NR	San Andres	0.003	0.01	2.75	21363	11882	21421	11797	0.27%	-0.72%
Column Averages				0.089	12.63	2.81	18167	10490	18899	10358	4.18%	-1.45%

Table 3
Dry Ultrasonic Velocities Measured at 2000 psid Differential Pressure
West Texas "Well A"

Sample No.	Approx. Wireline Depth (feet)	Res. (R) or Non-Res. (NR)	Stratigraphic Interval	Porosity (fraction)	Perm. (mD)	Grain Density (g/cc)	Dry Density (g/cc)	Dry Measurements				
								Vp (ft/s)	Vs (ft/s)	Bulk, Kd (GPa)	Shear, Gd (GPa)	P-Wave, Pd (GPa)
1V	2,797.0	R	E to D5	0.120	1.08	2.85	2.50	17926	10407	41.16	25.20	74.76
2V	2,810.5	NR	E to D5	0.005	0.01	2.73	2.71	19263	11117	52.00	31.16	93.54
3H	2,831.0	NR	E to D5	0.013	0.01	2.81	2.77	21466	11823	70.62	35.97	118.59
3V	2,831.0	NR	E to D5	0.012	0.01	2.80	2.77	20744	11683	63.90	35.12	110.73
4V	2,837.0	NR	E to D5	0.010	0.01	2.86	2.83	18853	10992	51.13	31.79	93.52
5V	2,868.0	R	D5 to M	0.214	53.10	2.84	2.23	14809	8471	25.66	14.89	45.51
6H	2,890.0	R	D5 to M	0.155	41.10	2.85	2.41	17914	10049	41.73	22.62	71.89
6V	2,890.0	R	D5 to M	0.217	53.90	2.85	2.23	13289	8146	18.25	13.74	36.56
7V	2,910.0	R	D5 to M	0.137	16.90	2.79	2.41	16397	9830	31.30	21.60	60.11
8H	2,914.0	R	D5 to M	0.154	17.00	2.84	2.41	18414	10546	42.66	24.87	75.82
8V	2,914.0	R	D5 to M	0.221	66.70	2.85	2.22	15136	9231	23.85	17.60	47.31
9V	2,933.0	R	D5 to M	0.123	2.56	2.78	2.44	18027	10556	39.99	25.26	73.67
10V	2,944.0	R	D5 to M	0.072	0.06	2.82	2.61	19794	11320	53.63	31.11	95.11
11V	2,956.0	NR	M to S.A.	0.079	0.04	2.83	2.60	17923	10603	41.43	27.18	77.67
12V	2,999.0	R	M to S.A.	0.082	0.07	2.78	2.55	17319	10073	39.00	24.03	71.05
13V	3,016.0	NR	M to S.A.	0.050	0.01	2.87	2.73	18842	10957	49.40	30.42	89.97
14H	3,026.0	R	M to S.A.	0.034	0.01	2.72	2.63	19444	10828	54.13	28.62	92.29
14V	3,026.0	R	M to S.A.	0.047	0.01	2.75	2.62	18558	10686	46.79	27.81	83.86
15V	3,038.5	NR	M to S.A.	0.027	0.01	2.88	2.80	17856	10602	43.95	29.24	82.93
16V	3,048.5	NR	San Andres	0.003	0.01	2.75	2.75	21363	11882	68.40	36.02	116.42
Column Averages				0.089	12.63	2.81	2.56	18167	10490	44.95	26.71	80.57

Table 4
Comparison of Measured-vs.-Gassmann Brine Effect at 2000 psid
West Texas "Well A"

Sample No.	Porosity (fraction)	Grain Density (g/cc)	Dry Measurements		Brine-Saturated Measurements		Measured Brine Effect		Dry P-wave Modulus (GPa)	Dry Shear Modulus (GPa)	Dry Bulk Modulus (GPa)	Grain Bulk Modulus (GPa)	Gassmann Brine		Gassmann-predicted Brine Effect	
			Vp (ft/s)	Vs (ft/s)	Vp (ft/s)	Vs (ft/s)	ΔVp	ΔVs					Vp (ft/s)	Vs (ft/s)	ΔVp	ΔVs
1V	0.120	2.85	17926	10407	18436	10382	2.85%	-0.24%	74.76	25.20	41.16	78.31	17992	10159	0.37%	-2.38%
2V	0.005	2.73	19263	11117	19309	11019	0.24%	-0.88%	93.54	31.16	52.00	73.14	20654	11106	7.22%	-0.09%
3H	0.013	2.81	21466	11823	21466	11563	0.00%	-2.20%	118.59	35.97	70.62	76.54	21506	11795	0.18%	-0.24%
3V	0.012	2.80	20744	11683	20929	11625	0.89%	-0.50%	110.73	35.12	63.90	76.46	21061	11657	1.53%	-0.23%
4V	0.010	2.86	18853	10992	20428	11210	8.35%	1.98%	93.52	31.79	51.13	78.89	20264	10972	7.48%	-0.18%
5V	0.214	2.84	14809	8471	15022	8103	1.44%	-4.34%	45.51	14.89	25.66	78.04	14877	8083	0.46%	-4.58%
6H	0.155	2.85	17914	10049	18305	9910	2.18%	-1.38%	71.89	22.62	41.73	78.61	17747	9732	-0.93%	-3.15%
6V	0.217	2.85	13289	8146	14179	7535	6.70%	-7.50%	36.56	13.74	18.25	78.26	13714	7767	3.20%	-4.66%
7V	0.137	2.79	16397	9830	17944	9786	9.43%	-0.45%	60.11	21.60	31.30	75.75	16674	9555	1.69%	-2.80%
8H	0.154	2.84	18414	10546	19094	10467	3.69%	-0.75%	75.82	24.87	42.66	78.16	18206	10216	-1.13%	-3.13%
8V	0.221	2.85	15136	9231	15785	8153	4.29%	-11.68%	47.31	17.60	23.85	78.61	15179	8792	0.28%	-4.75%
9V	0.123	2.78	18027	10556	18735	10280	3.93%	-2.61%	73.67	25.26	39.99	75.58	18059	10292	0.18%	-2.50%
10V	0.072	2.82	19794	11320	20569	11379	3.92%	0.52%	95.11	31.11	53.63	76.95	19814	11163	0.10%	-1.39%
11V	0.079	2.83	17923	10603	19193	10695	7.09%	0.87%	77.67	27.18	41.43	77.42	18307	10441	2.14%	-1.53%
12V	0.082	2.78	17319	10073	18431	9932	6.42%	-1.40%	71.05	24.03	39.00	75.36	17753	9910	2.50%	-1.62%
13V	0.050	2.87	18842	10957	20042	11033	6.37%	0.69%	89.97	30.42	49.40	79.31	19273	10856	2.29%	-0.92%
14H	0.034	2.72	19444	10828	19705	10716	1.34%	-1.03%	92.29	28.62	54.13	72.79	19729	10757	1.47%	-0.65%
14V	0.047	2.75	18558	10686	19213	10807	3.53%	1.13%	83.86	27.81	46.79	74.11	19026	10589	2.52%	-0.90%
15V	0.027	2.88	17856	10602	19769	10768	10.71%	1.57%	82.93	29.24	43.95	79.56	19070	10551	6.80%	-0.48%
16V	0.003	2.75	21363	11882	21421	11797	0.27%	-0.72%	116.42	36.02	68.40	74.29	21613	11876	1.17%	-0.05%
Column Averages			18167	10490	18899	10358	4.18%	-1.45%	80.57	26.71	44.95	76.81	18526	10313	1.98%	-1.81%

Appendix A

Plots of Ultrasonic Data for Each Plug Sample

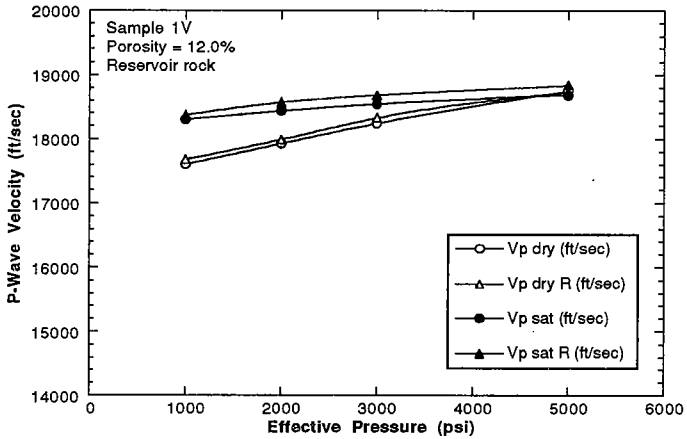
Sample 1V
Porosity = 12.0%
Reservoir rock
P-Wave Velocity (ft/sec)
Effective Pressure (psi)
Vp dry (ft/sec)
Vp dry R (ft/sec)
Vp sat (ft/sec)
Vp sat R (ft/sec)

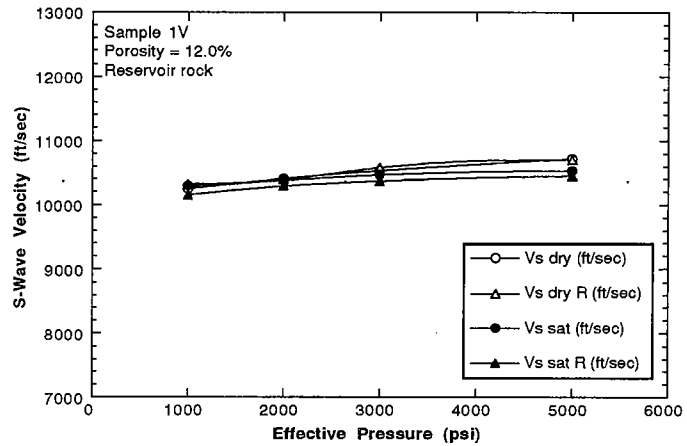
Sample 1V
Porosity = 12.0%
Reservoir rock
S-Wave Velocity (ft/sec)
Effective Pressure (psi)
Vs dry (ft/sec)
Vs dry R (ft/sec)
Vs sat (ft/sec)
Vs sat R (ft/sec)

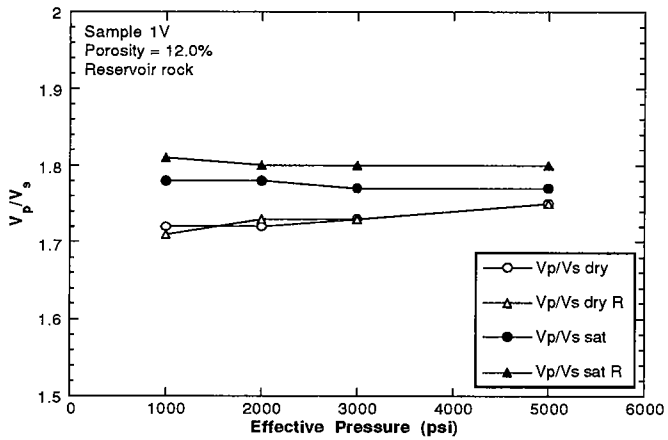
Sample 1V
Porosity = 12.0%
Reservoir rock
Vp/Vs
Effective Pressure (psi)
Vp/Vs dry
Vp/Vs dry R
Vp/Vs sat
Vp/Vs sat R

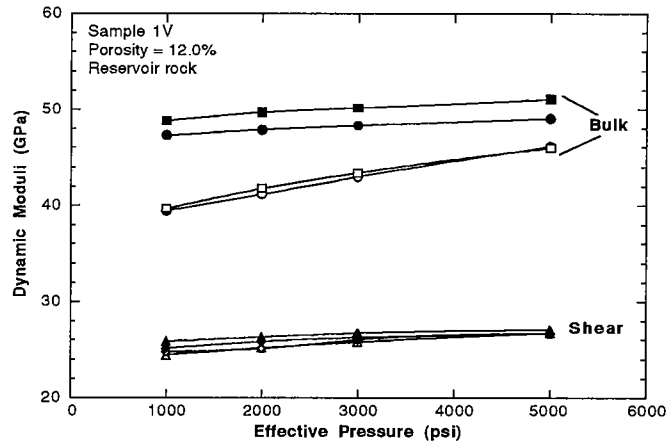
Sample 1V
Porosity = 12.0%
Reservoir rock
Dynamic Moduli (GPa)
Effective Pressure (psi)
Bulk
Shear

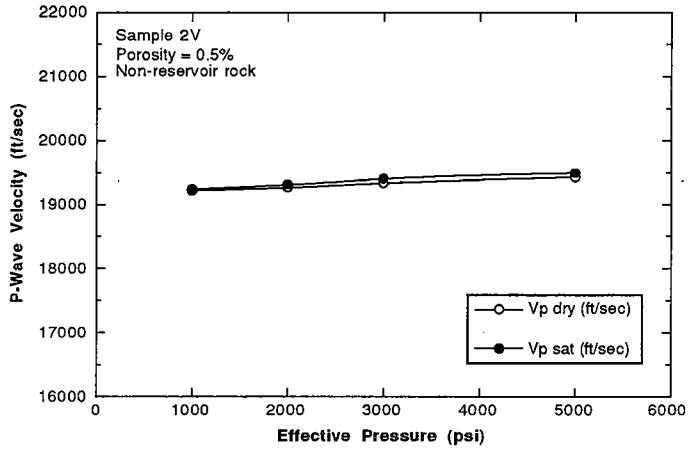
Sample 2V
Porosity = 0.5%
Non-reservoir rock
Vp dry (ft/sec)
Vp sat (ft/sec)
P-Wave Velocity (ft/sec)
Effective Pressure (psi)
22000
21000
20000
19000
18000
17000
16000
0
1000
2000
3000
4000
5000
6000

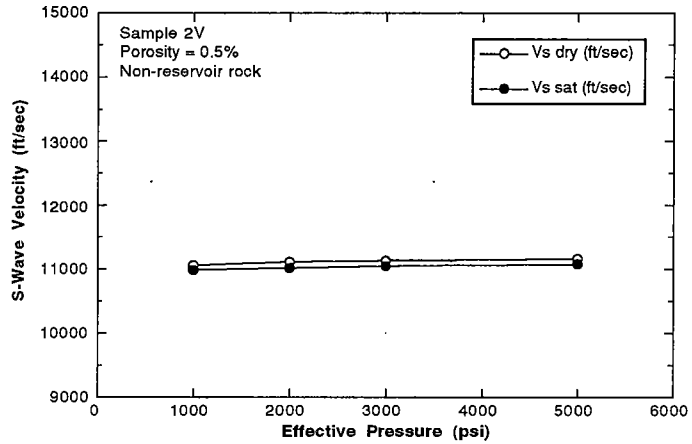
Sample 2V
Porosity = 0.5%
Non-reservoir rock
Vs dry (ft/sec)
Vs sat (ft/sec)
S-Wave Velocity (ft/sec)
Effective Pressure (psi)
15000
14000
13000
12000
11000
10000
9000
0
1000
2000
3000
4000
5000
6000

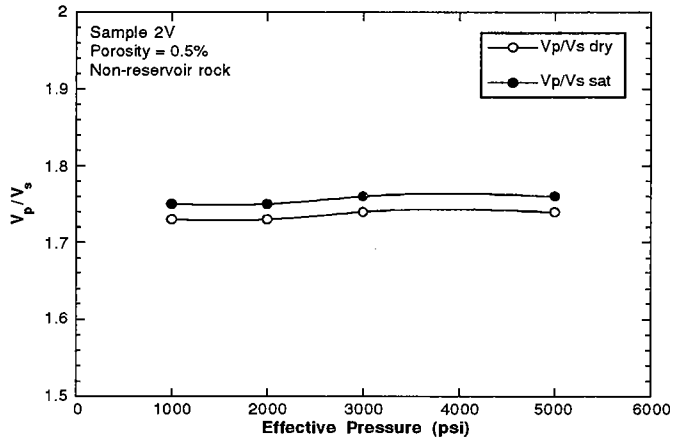
Sample 2V
Porosity = 0.5%
Non-reservoir rock
Vp/Vs dry
Vp/Vs sat
Vp/Vs
Effective Pressure (psi)
2
1.9
1.8
1.7
1.6
1.5
0
1000
2000
3000
4000
5000
6000

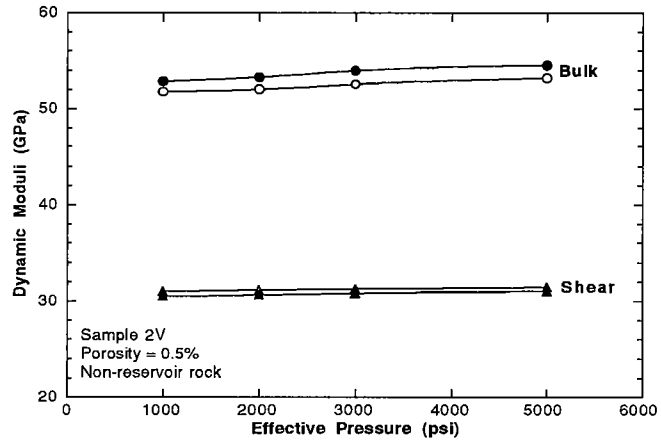
Bulk
Shear
Sample 2V
Porosity = 0.5%
Non-reservoir rock
Dynamic Moduli (GPa)
Effective Pressure (psi)
60
50
40
30
20
0
1000
2000
3000
4000
5000
6000

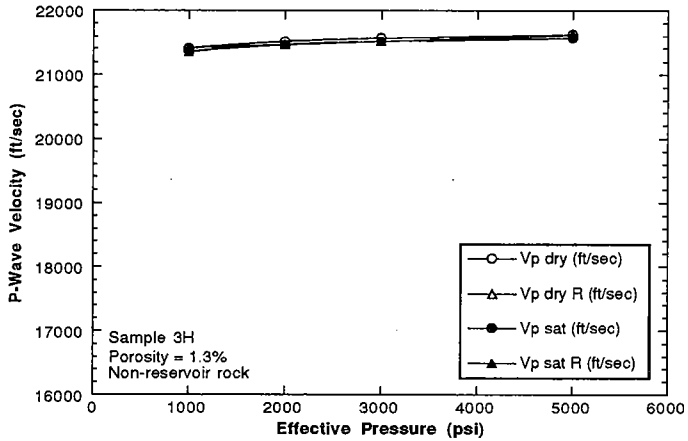
P-Wave Velocity (ft/sec)
Effective Pressure (psi)
Sample 3H
Porosity = 1.3%
Non-reservoir rock
Vp dry (ft/sec)
Vp dry R (ft/sec)
Vp sat (ft/sec)
Vp sat R (ft/sec)

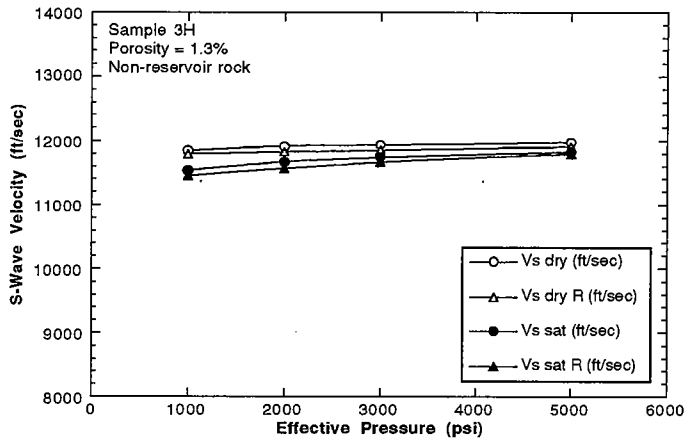
S-Wave Velocity (ft/sec)
Effective Pressure (psi)
Sample 3H
Porosity = 1.3%
Non-reservoir rock
Vs dry (ft/sec)
Vs dry R (ft/sec)
Vs sat (ft/sec)
Vs sat R (ft/sec)

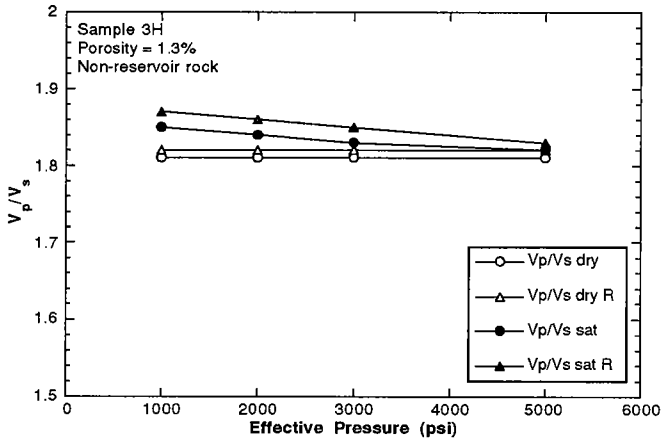
Vp/Vs
Effective Pressure (psi)
Sample 3H
Porosity = 1.3%
Non-reservoir rock
Vp/Vs dry
Vp/Vs dry R
Vp/Vs sat
Vp/Vs sat R

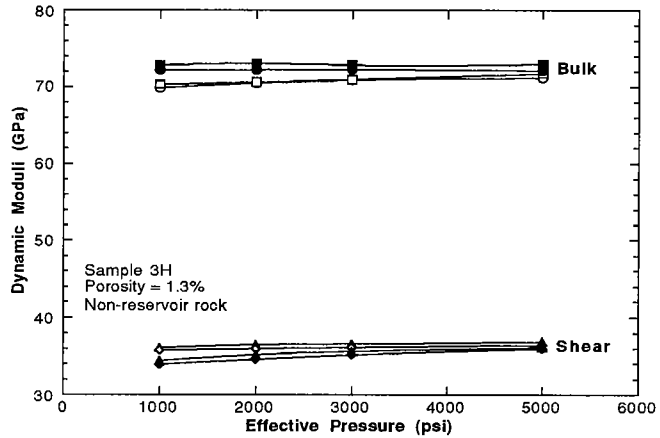
Dynamic Moduli (GPa)
Effective Pressure (psi)
Sample 3H
Porosity = 1.3%
Non-reservoir rock
Bulk
Shear

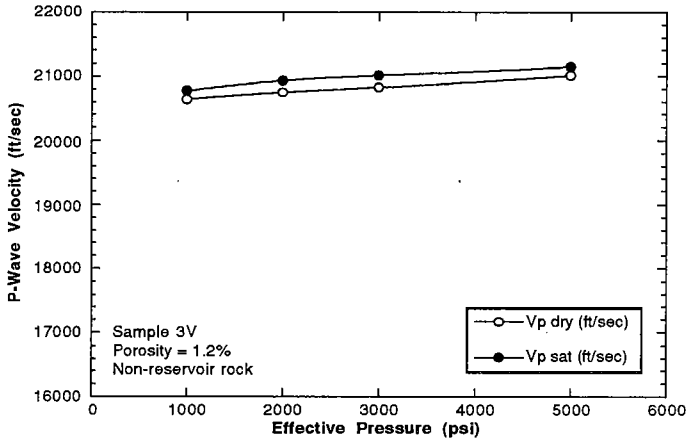
P-Wave Velocity (ft/sec)
Effective Pressure (psi)
Sample 3V
Porosity = 1.2%
Non-reservoir rock
Vp dry (ft/sec)
Vp sat (ft/sec)

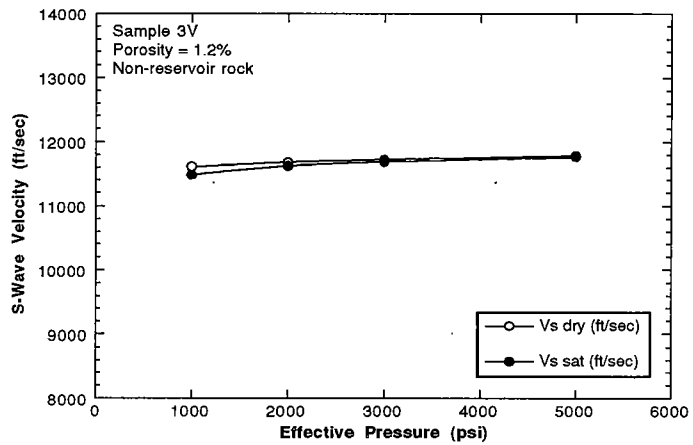
S-Wave Velocity (ft/sec)
Effective Pressure (psi)
Sample 3V
Porosity = 1.2%
Non-reservoir rock
Vs dry (ft/sec)
Vs sat (ft/sec)

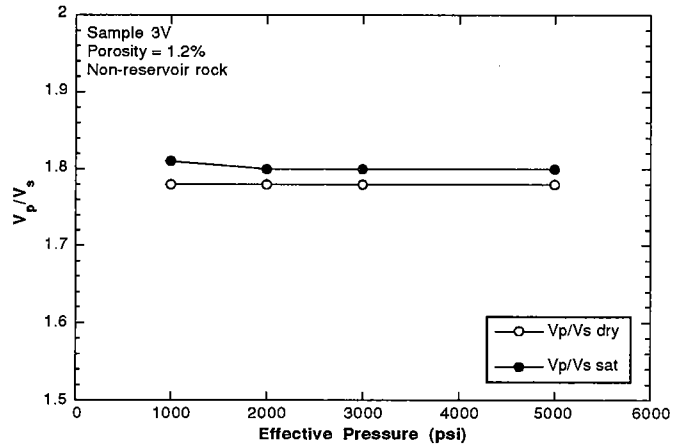
Vp/Vs
Effective Pressure (psi)
Sample 3V
Porosity = 1.2%
Non-reservoir rock
Vp/Vs dry
Vp/Vs sat

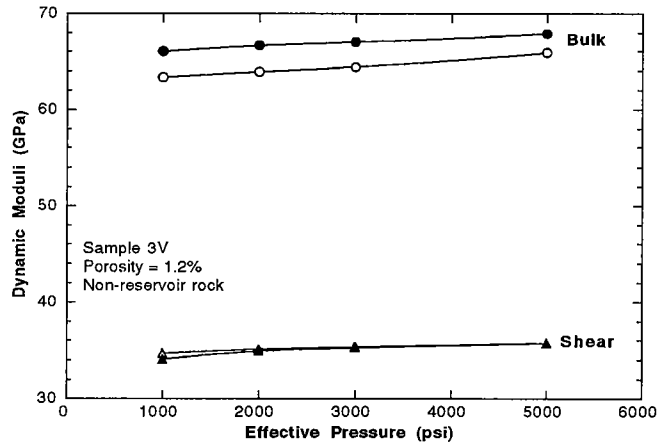
Dynamic Moduli (GPa)
Effective Pressure (psi)
Sample 3V
Porosity = 1.2%
Non-reservoir rock
Bulk
Shear

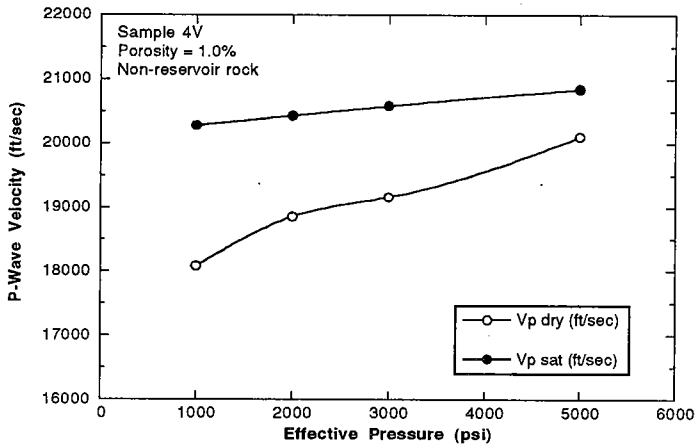
Sample 4V
Porosity = 1.0%
Non-reservoir rock
Vp dry (ft/sec)
Vp sat (ft/sec)
P-Wave Velocity (ft/sec)
Effective Pressure (psi)
22000
21000
20000
19000
18000
17000
16000
0
1000
2000
3000
4000
5000
6000

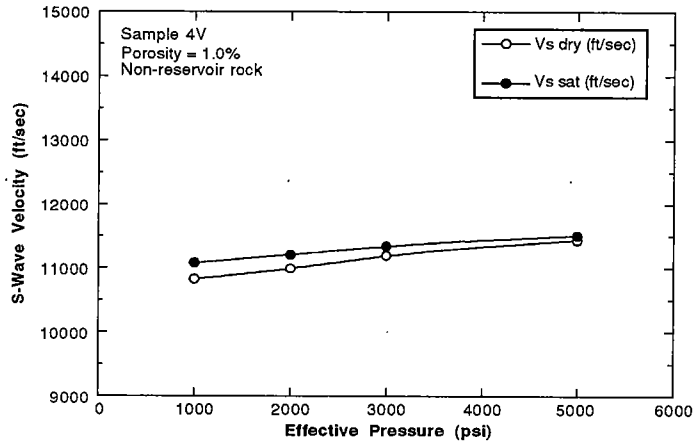
Sample 4V
Porosity = 1.0%
Non-reservoir rock
Vs dry (ft/sec)
Vs sat (ft/sec)
S-Wave Velocity (ft/sec)
Effective Pressure (psi)
15000
14000
13000
12000
11000
10000
9000
0
1000
2000
3000
4000
5000
6000

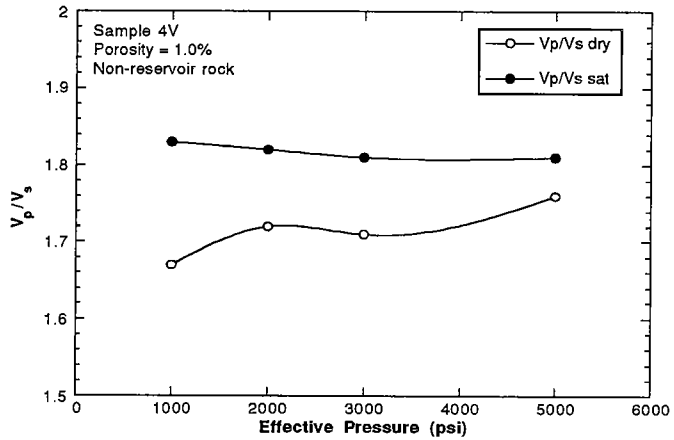
Sample 4V
Porosity = 1.0%
Non-reservoir rock
Vp/Vs dry
Vp/Vs sat
Vp/Vs
Effective Pressure (psi)
2
1.9
1.8
1.7
1.6
1.5
0
1000
2000
3000
4000
5000
6000

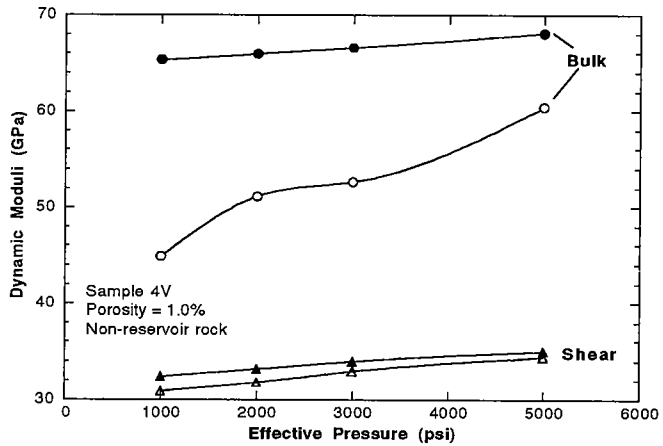
Bulk
Shear
Sample 4V
Porosity = 1.0%
Non-reservoir rock
Dynamic Moduli (GPa)
Effective Pressure (psi)
70
60
50
40
30
0
1000
2000
3000
4000
5000
6000

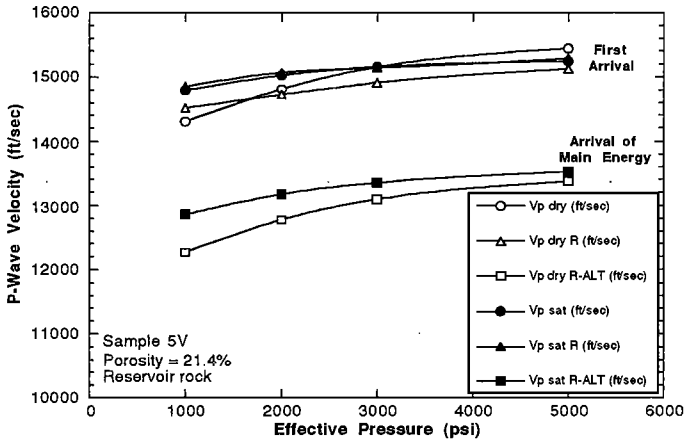
P-Wave Velocity (ft/sec)
Effective Pressure (psi)
First Arrival
Arrival of Main Energy
Vp dry (ft/sec)
Vp dry R (ft/sec)
Vp dry R-ALT (ft/sec)
Vp sat (ft/sec)
Vp sat R (ft/sec)
Vp sat R-ALT (ft/sec)
Sample 5V
Porosity = 21.4%
Reservoir rock

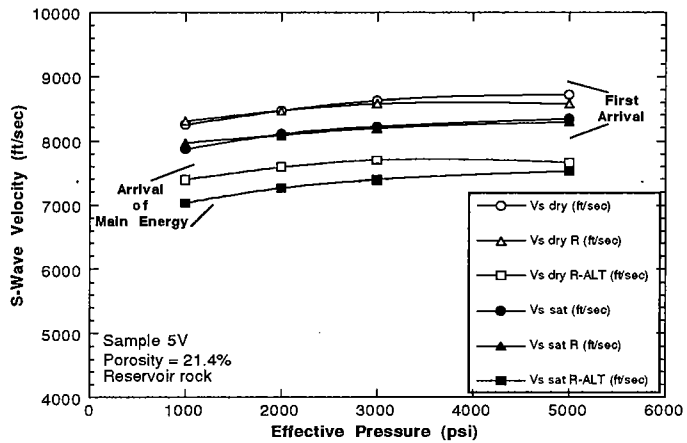
S-Wave Velocity (ft/sec)
Effective Pressure (psi)
First Arrival
Arrival of Main Energy
Vs dry (ft/sec)
Vs dry R (ft/sec)
Vs dry R-ALT (ft/sec)
Vs sat (ft/sec)
Vs sat R (ft/sec)
Vs sat R-ALT (ft/sec)
Sample 5V
Porosity = 21.4%
Reservoir rock

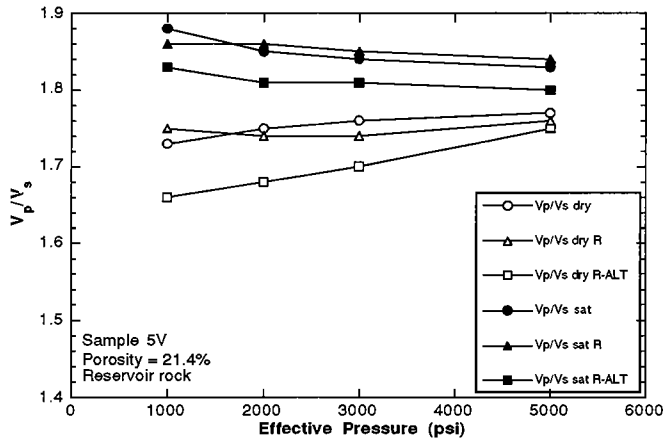
Vp/Vs
Effective Pressure (psi)
Vp/Vs dry
Vp/Vs dry R
Vp/Vs dry R-ALT
Vp/Vs sat
Vp/Vs sat R
Vp/Vs sat R-ALT
Sample 5V
Porosity = 21.4%
Reservoir rock

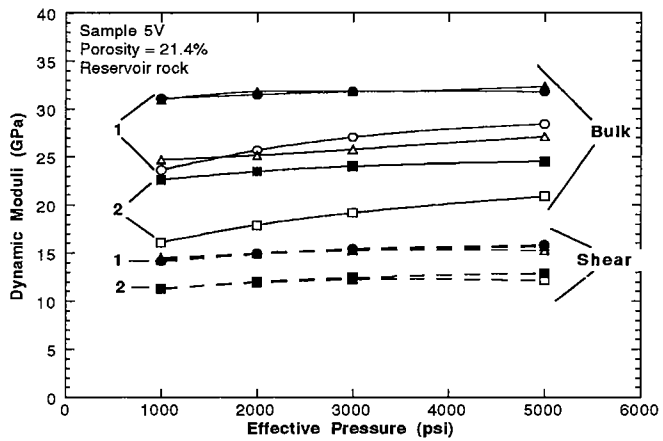
Dynamic Moduli (GPa)
Effective Pressure (psi)
Sample 5V
Porosity = 21.4%
Reservoir rock
Bulk
Shear
1
2
1
2

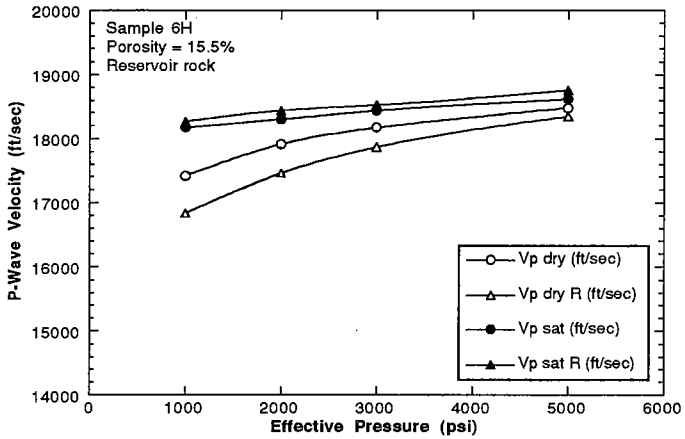
Sample 6H
Porosity = 15.5%
Reservoir rock
P-Wave Velocity (ft/sec)
Effective Pressure (psi)
Vp dry (ft/sec)
Vp dry R (ft/sec)
Vp sat (ft/sec)
Vp sat R (ft/sec)

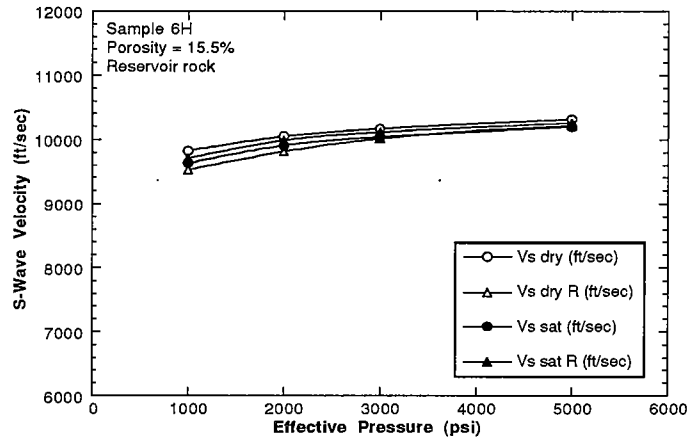
Sample 6H
Porosity = 15.5%
Reservoir rock
S-Wave Velocity (ft/sec)
Effective Pressure (psi)
Vs dry (ft/sec)
Vs dry R (ft/sec)
Vs sat (ft/sec)
Vs sat R (ft/sec)

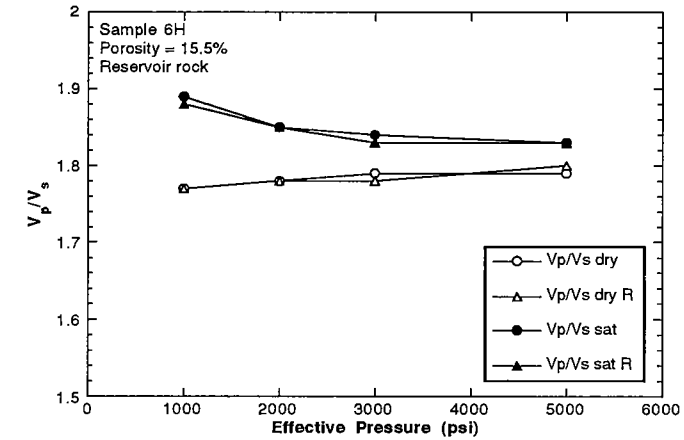
Sample 6H
Porosity = 15.5%
Reservoir rock
Vp/Vs
Effective Pressure (psi)
Vp/Vs dry
Vp/Vs dry R
Vp/Vs sat
Vp/Vs sat R

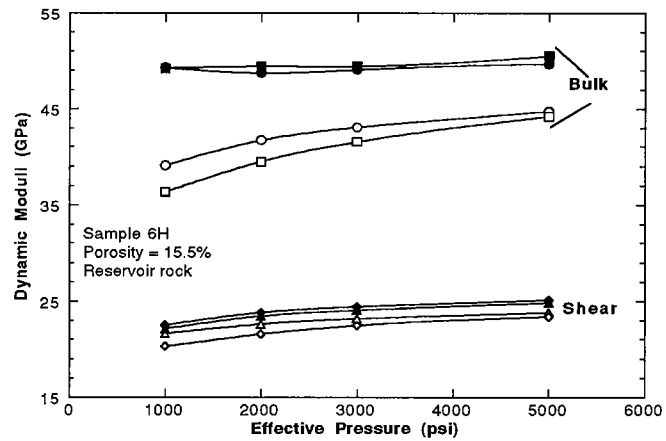
Sample 6H
Porosity = 15.5%
Reservoir rock
Dynamic Moduli (GPa)
Effective Pressure (psi)
Bulk
Shear

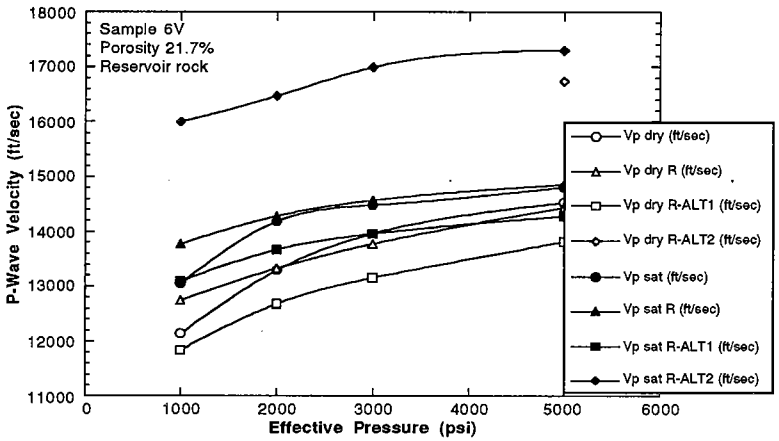
Sample 6V
Porosity 21.7%
Reservoir rock
P-Wave Velocity (ft/sec)
Effective Pressure (psi)
Vp dry (ft/sec)
Vp dry R (ft/sec)
Vp dry R-ALT1 (ft/sec)
Vp dry R-ALT2 (ft/sec)
Vp sat (ft/sec)
Vp sat R (ft/sec)
Vp sat R-ALT1 (ft/sec)
Vp sat R-ALT2 (ft/sec)

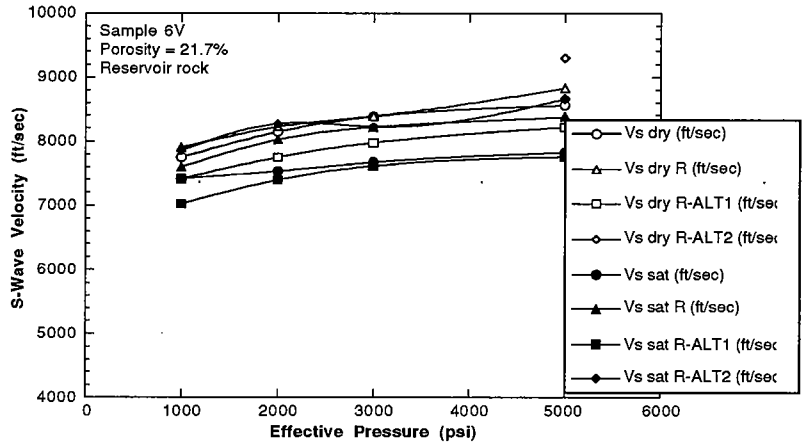
Sample 6V
Porosity = 21.7%
Reservoir rock
S-Wave Velocity (ft/sec)
Effective Pressure (psi)
Vs dry (ft/sec)
Vs dry R (ft/sec)
Vs dry R-ALT1 (ft/sec
Vs dry R-ALT2 (ft/sec
Vs sat (ft/sec)
Vs sat R (ft/sec)
Vs sat R-ALT1 (ft/sec
Vs sat R-ALT2 (ft/sec

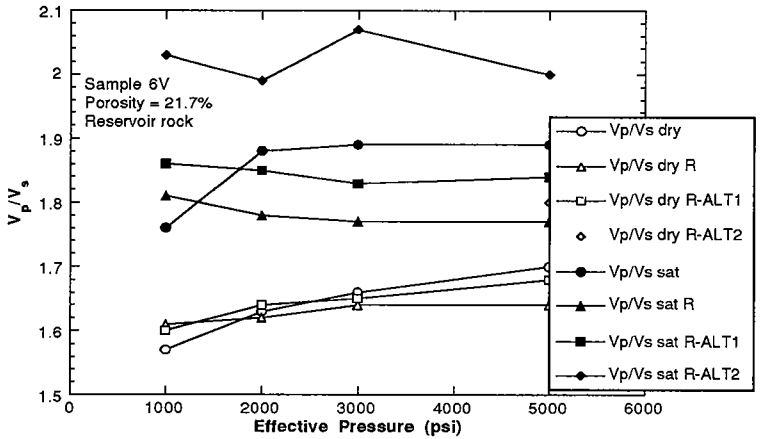
Sample 6V
Porosity = 21.7%
Reservoir rock
Vp/Vs
Effective Pressure (psi)
Vp/Vs dry
Vp/Vs dry R
Vp/Vs dry R-ALT1
Vp/Vs dry R-ALT2
Vp/Vs sat
Vp/Vs sat R
Vp/Vs sat R-ALT1
Vp/Vs sat R-ALT2

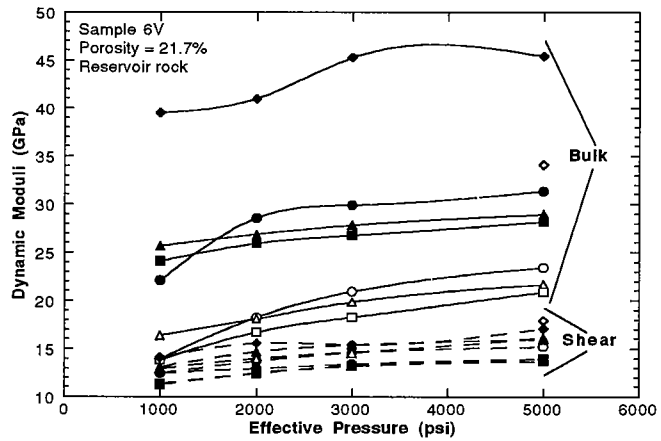
Sample 6V
Porosity = 21.7%
Reservoir rock
Dynamic Moduli (GPa)
Effective Pressure (psi)
Bulk
Shear

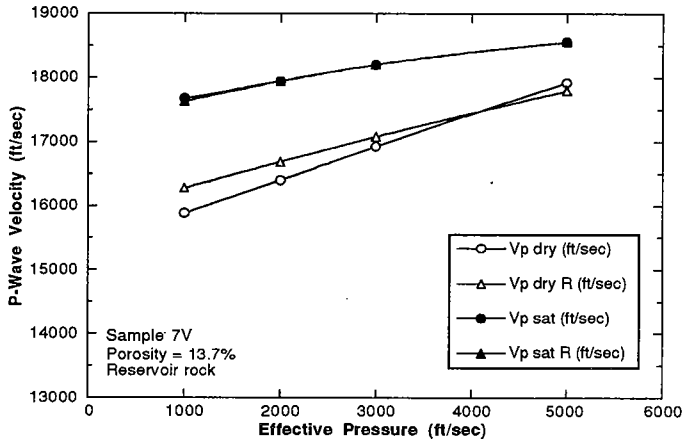
P-Wave Velocity (ft/sec)
Effective Pressure (ft/sec)
Sample 7V
Porosity = 13.7%
Reservoir rock
Vp dry (ft/sec)
Vp dry R (ft/sec)
Vp sat (ft/sec)
Vp sat R (ft/sec)

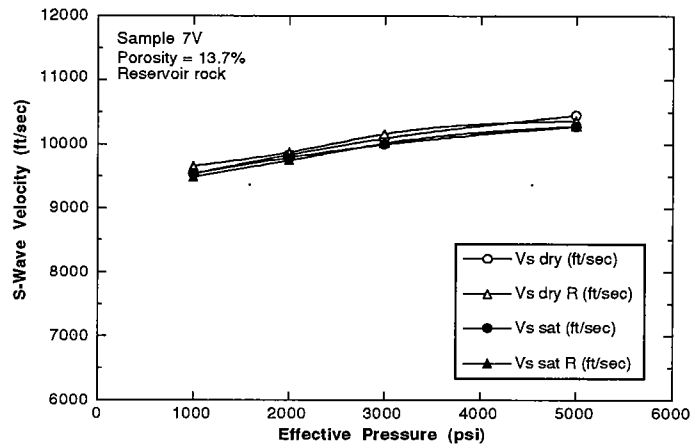
S-Wave Velocity (ft/sec)
Effective Pressure (psi)
Sample 7V
Porosity = 13.7%
Reservoir rock
Vs dry (ft/sec)
Vs dry R (ft/sec)
Vs sat (ft/sec)
Vs sat R (ft/sec)

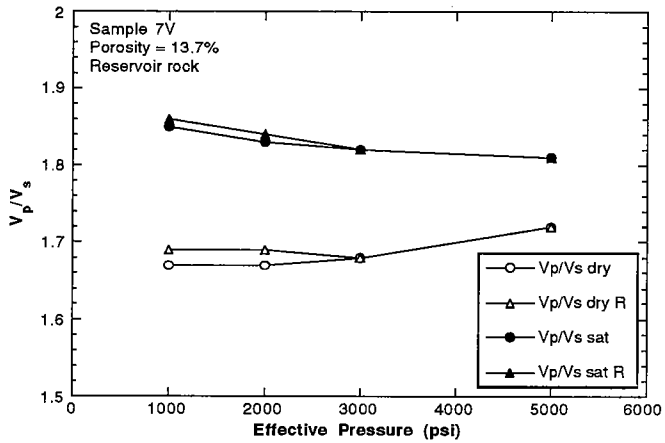
Vp/Vs
Effective Pressure (psi)
Sample 7V
Porosity = 13.7%
Reservoir rock
Vp/Vs dry
Vp/Vs dry R
Vp/Vs sat
Vp/Vs sat R

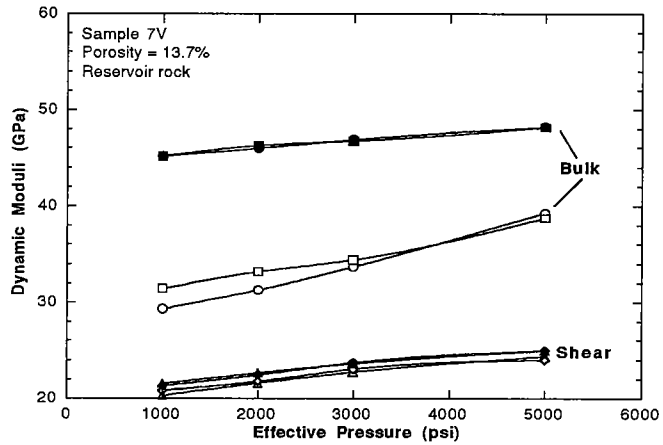
Dynamic Moduli (GPa)
Effective Pressure (psi)
Sample 7V
Porosity = 13.7%
Reservoir rock
Bulk
Shear

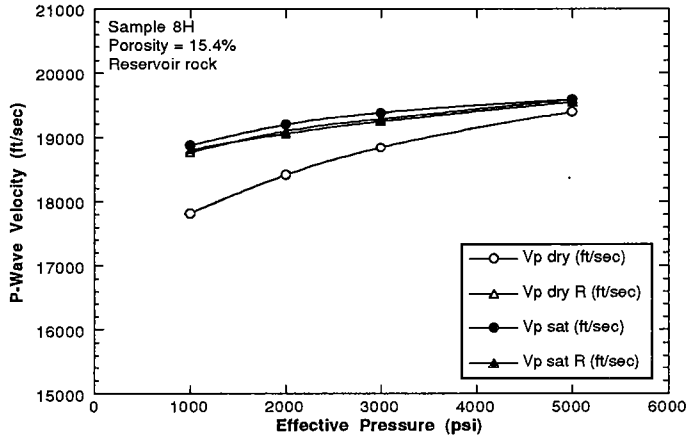
Sample 8H
Porosity = 15.4%
Reservoir rock
P-Wave Velocity (ft/sec)
Effective Pressure (psi)
Vp dry (ft/sec)
Vp dry R (ft/sec)
Vp sat (ft/sec)
Vp sat R (ft/sec)

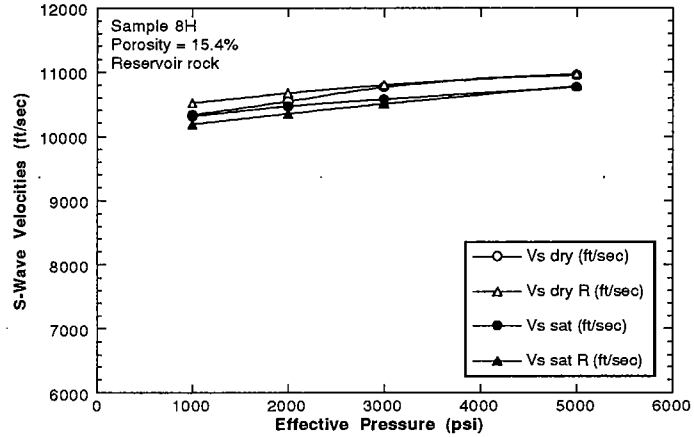
Sample 8H
Porosity = 15.4%
Reservoir rock
S-Wave Velocities (ft/sec)
Effective Pressure (psi)
Vs dry (ft/sec)
Vs dry R (ft/sec)
Vs sat (ft/sec)
Vs sat R (ft/sec)

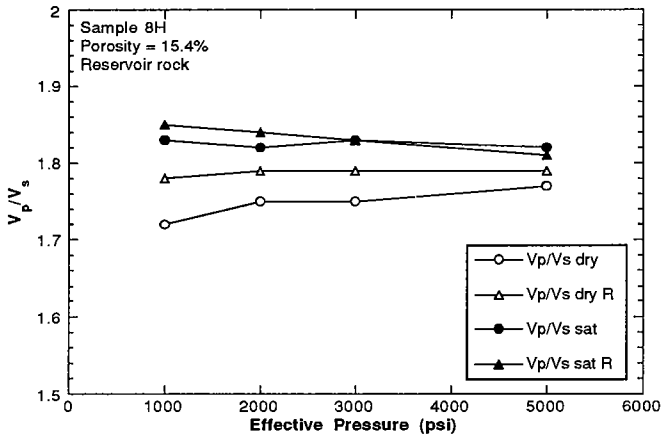
Sample 8H
Porosity = 15.4%
Reservoir rock
Vp/Vs
Effective Pressure (psi)
Vp/Vs dry
Vp/Vs dry R
Vp/Vs sat
Vp/Vs sat R

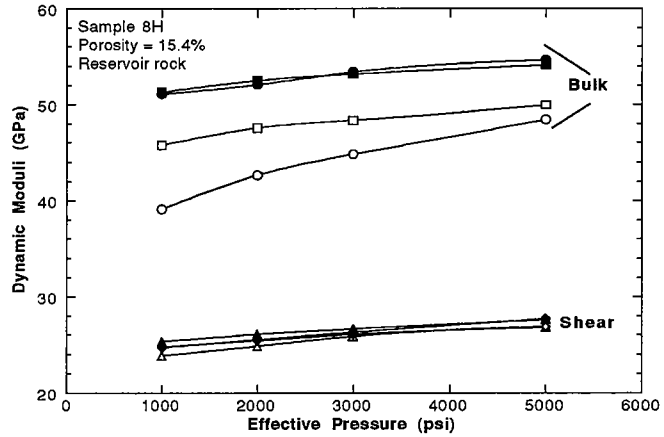
Sample 8H
Porosity = 15.4%
Reservoir rock
Dynamic Moduli (GPa)
Effective Pressure (psi)
Bulk
Shear

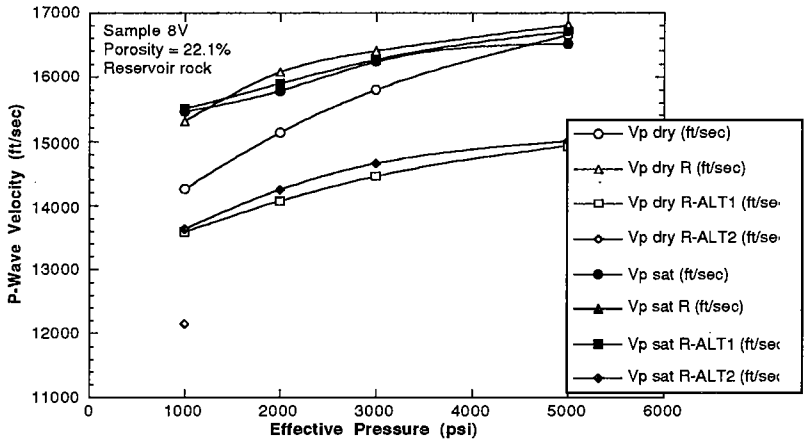
Sample 8V
Porosity = 22.1%
Reservoir rock
P-Wave Velocity (ft/sec)
Effective Pressure (psi)
Vp dry (ft/sec)
Vp dry R (ft/sec)
Vp dry R-ALT1 (ft/se
Vp dry R-ALT2 (ft/se
Vp sat (ft/sec)
Vp sat R (ft/sec)
Vp sat R-ALT1 (ft/se
Vp sat R-ALT2 (ft/se

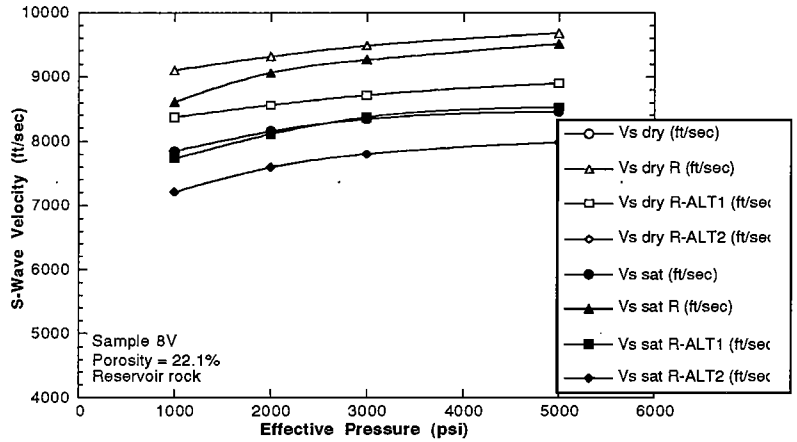
Sample 8V
Porosity = 22.1%
Reservoir rock
S-Wave Velocity (ft/sec)
Effective Pressure (psi)
Vs dry (ft/sec)
Vs dry R (ft/sec)
Vs dry R-ALT1 (ft/se
Vs dry R-ALT2 (ft/se
Vs sat (ft/sec)
Vs sat R (ft/sec)
Vs sat R-ALT1 (ft/se
Vs sat R-ALT2 (ft/se

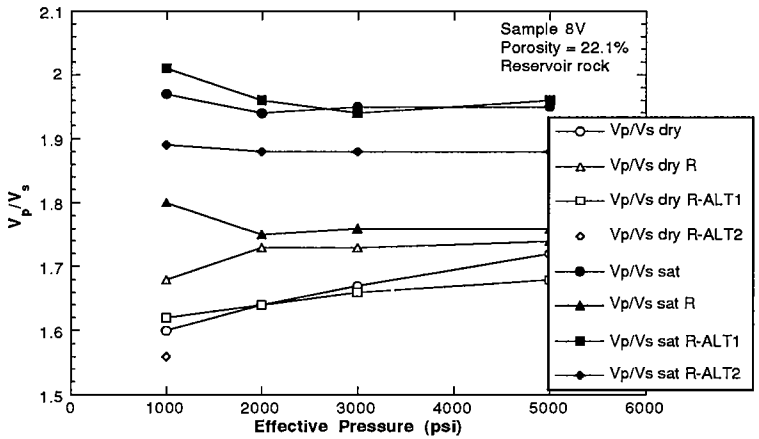
Sample 8V
Porosity = 22.1%
Reservoir rock
Vp/Vs
Effective Pressure (psi)
Vp/Vs dry
Vp/Vs dry R
Vp/Vs dry R-ALT1
Vp/Vs dry R-ALT2
Vp/Vs sat
Vp/Vs sat R
Vp/Vs sat R-ALT1
Vp/Vs sat R-ALT2

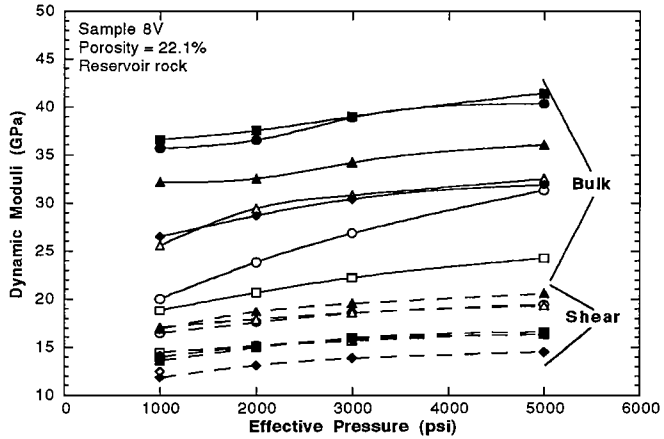
Sample 8V
Porosity = 22.1%
Reservoir rock
Dynamic Moduli (GPa)
Effective Pressure (psi)
Bulk
Shear

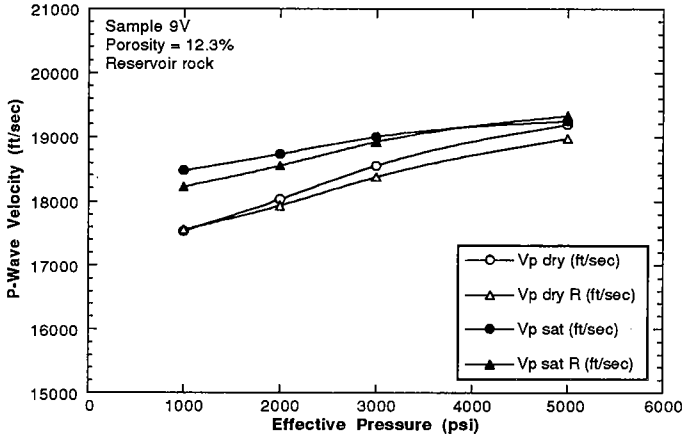
Sample 9V
Porosity = 12.3%
Reservoir rock
P-Wave Velocity (ft/sec)
Effective Pressure (psi)
Vp dry (ft/sec)
Vp dry R (ft/sec)
Vp sat (ft/sec)
Vp sat R (ft/sec)

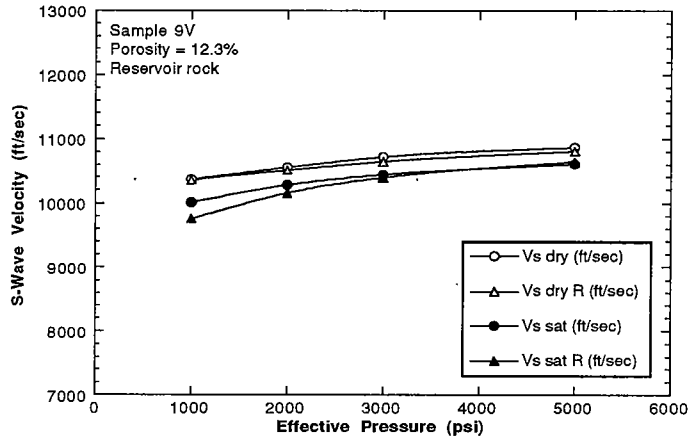
Sample 9V
Porosity = 12.3%
Reservoir rock
S-Wave Velocity (ft/sec)
Effective Pressure (psi)
Vs dry (ft/sec)
Vs dry R (ft/sec)
Vs sat (ft/sec)
Vs sat R (ft/sec)

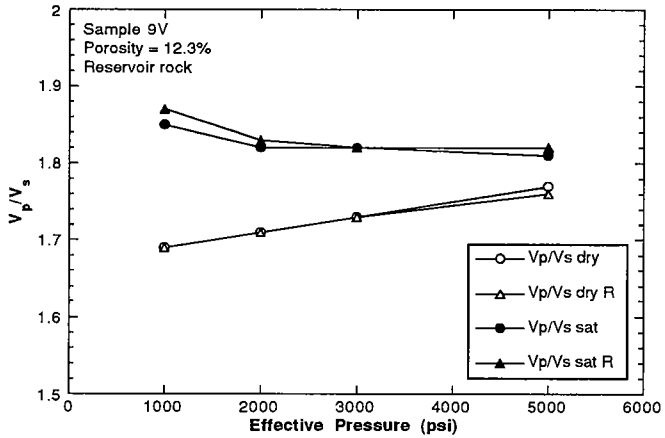
Sample 9V
Porosity = 12.3%
Reservoir rock
Vp/Vs
Effective Pressure (psi)
Vp/Vs dry
Vp/Vs dry R
Vp/Vs sat
Vp/Vs sat R

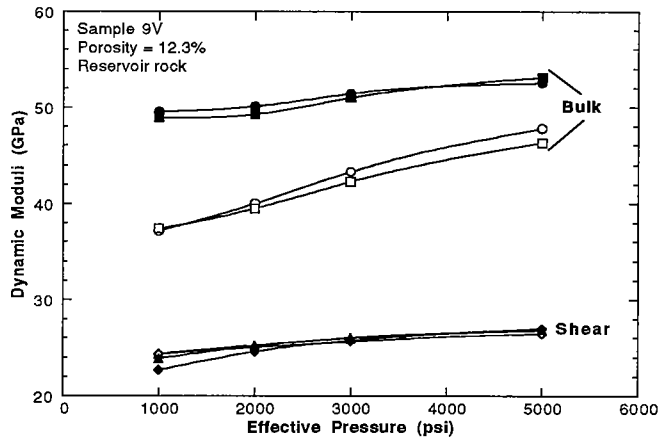
Sample 9V
Porosity = 12.3%
Reservoir rock
Dynamic Moduli (GPa)
Effective Pressure (psi)
Bulk
Shear

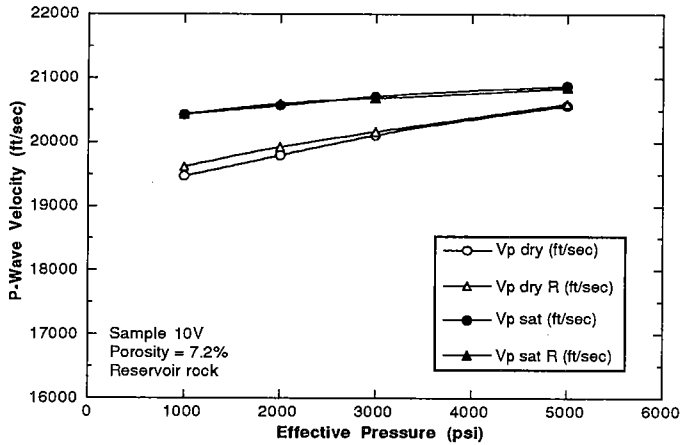
P-Wave Velocity (ft/sec)
Effective Pressure (psi)
Sample 10V
Porosity = 7.2%
Reservoir rock
Vp dry (ft/sec)
Vp dry R (ft/sec)
Vp sat (ft/sec)
Vp sat R (ft/sec)

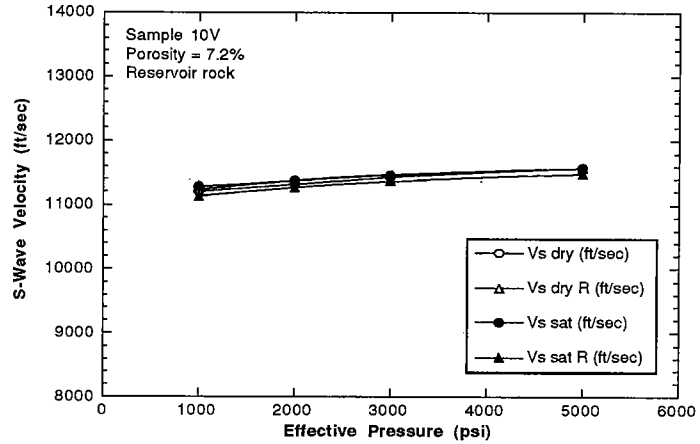
S-Wave Velocity (ft/sec)
Effective Pressure (psi)
Sample 10V
Porosity = 7.2%
Reservoir rock
Vs dry (ft/sec)
Vs dry R (ft/sec)
Vs sat (ft/sec)
Vs sat R (ft/sec)

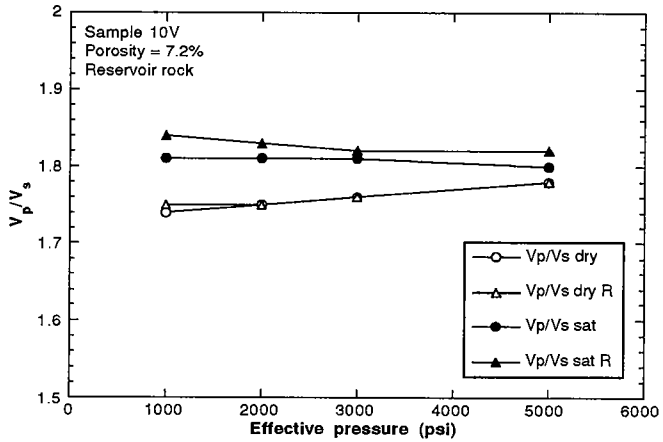
Vp/Vs
Effective pressure (psi)
Sample 10V
Porosity = 7.2%
Reservoir rock
Vp/Vs dry
Vp/Vs dry R
Vp/Vs sat
Vp/Vs sat R

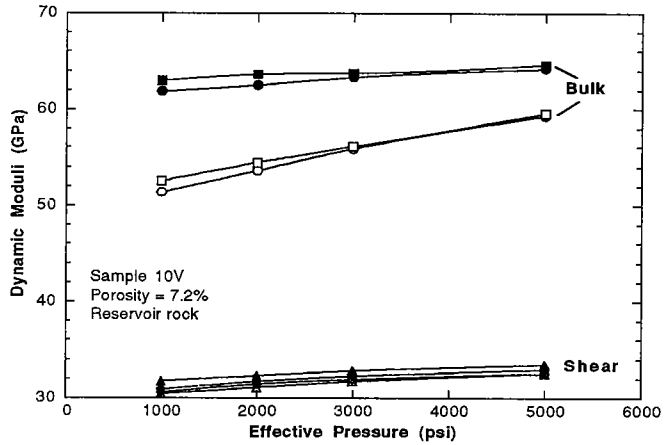
Dynamic Moduli (GPa)
Effective Pressure (psi)
Sample 10V
Porosity = 7.2%
Reservoir rock
Bulk
Shear

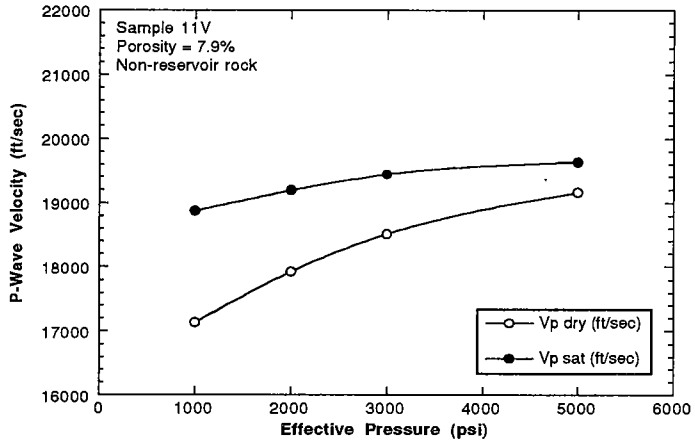
Sample 11V
Porosity = 7.9%
Non-reservoir rock
P-Wave Velocity (ft/sec)
Effective Pressure (psi)
Vp dry (ft/sec)
Vp sat (ft/sec)

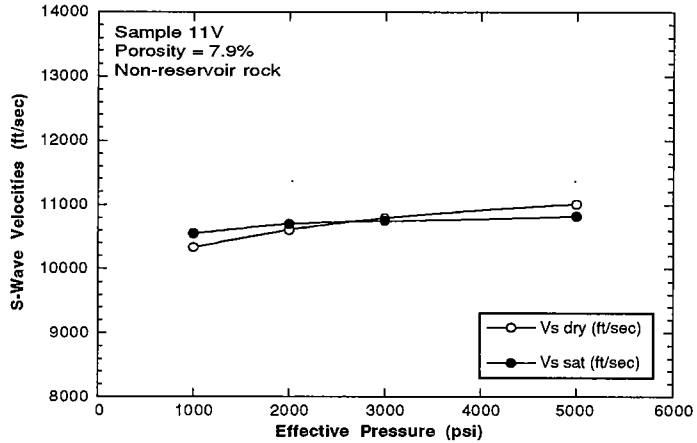
Sample 11V
Porosity = 7.9%
Non-reservoir rock
S-Wave Velocities (ft/sec)
Effective Pressure (psi)
Vs dry (ft/sec)
Vs sat (ft/sec)

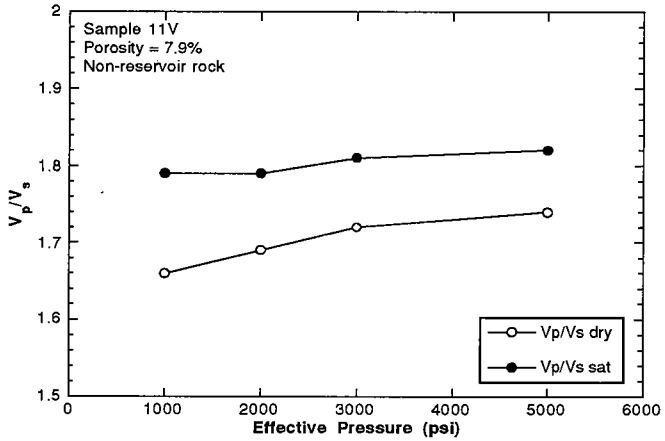
Sample 11V
Porosity = 7.9%
Non-reservoir rock
Vp/Vs
Effective Pressure (psi)
Vp/Vs dry
Vp/Vs sat

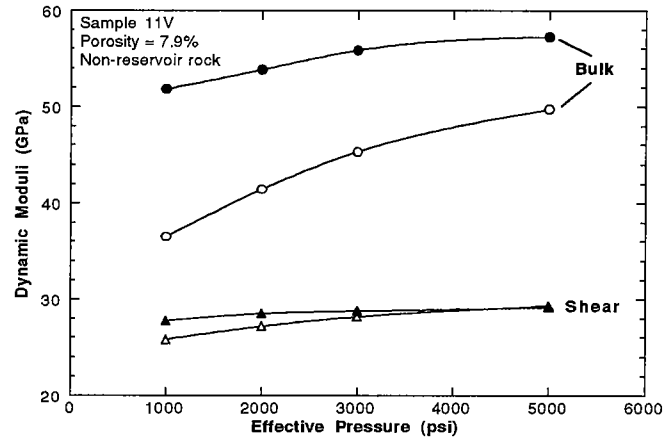
Sample 11V
Porosity = 7.9%
Non-reservoir rock
Dynamic Moduli (GPa)
Effective Pressure (psi)
Bulk
Shear

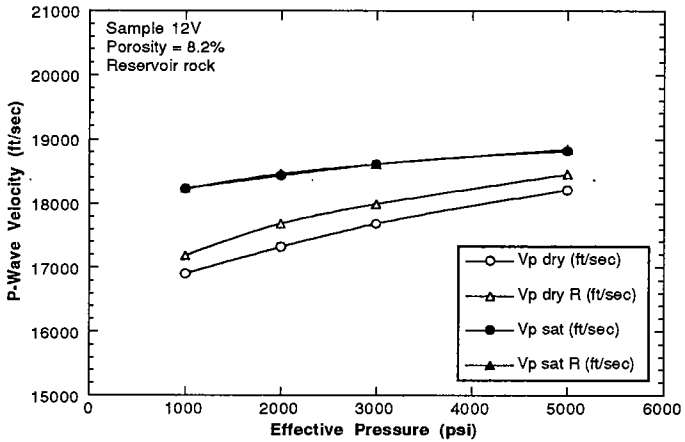
Sample 12V
Porosity = 8.2%
Reservoir rock
P-Wave Velocity (ft/sec)
Effective Pressure (psi)
Vp dry (ft/sec)
Vp dry R (ft/sec)
Vp sat (ft/sec)
Vp sat R (ft/sec)

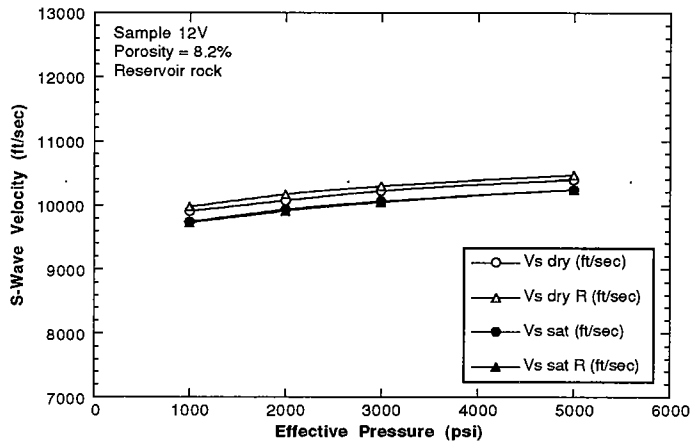
Sample 12V
Porosity = 8.2%
Reservoir rock
S-Wave Velocity (ft/sec)
Effective Pressure (psi)
Vs dry (ft/sec)
Vs dry R (ft/sec)
Vs sat (ft/sec)
Vs sat R (ft/sec)

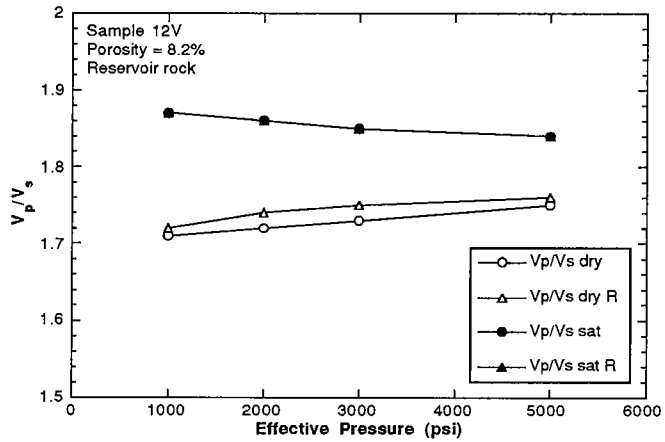
Sample 12V
Porosity = 8.2%
Reservoir rock
Vp/Vs
Effective Pressure (psi)
Vp/Vs dry
Vp/Vs dry R
Vp/Vs sat
Vp/Vs sat R

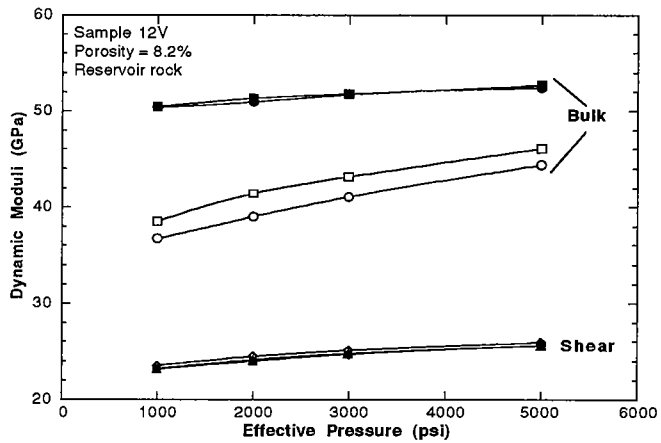
Sample 12V
Porosity = 8.2%
Reservoir rock
Dynamic Moduli (GPa)
Effective Pressure (psi)
Bulk
Shear

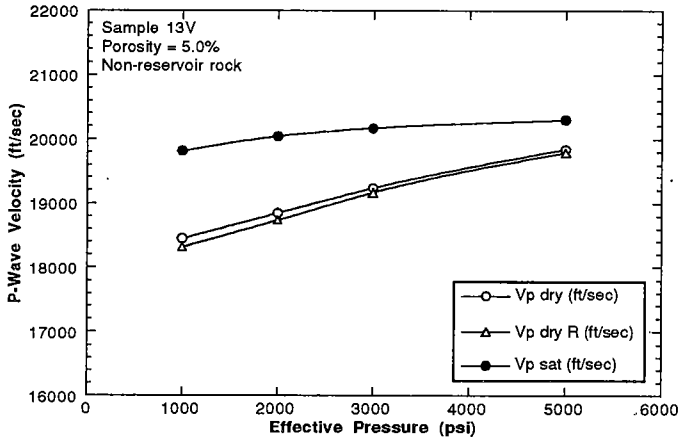
Sample 13V
Porosity = 5.0%
Non-reservoir rock
P-Wave Velocity (ft/sec)
Effective Pressure (psi)
Vp dry (ft/sec)
Vp dry R (ft/sec)
Vp sat (ft/sec)

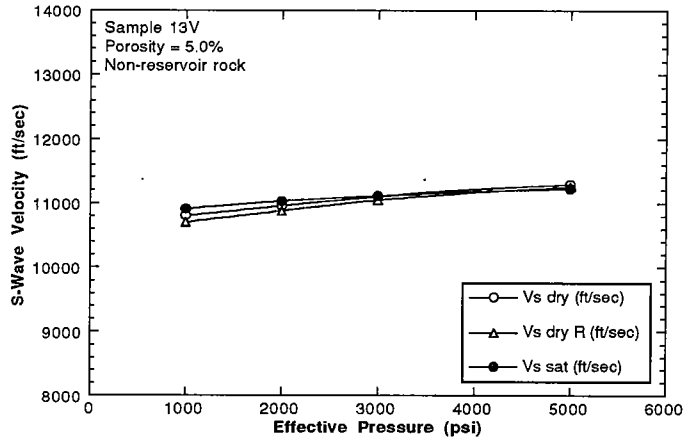
Sample 13V
Porosity = 5.0%
Non-reservoir rock
S-Wave Velocity (ft/sec)
Effective Pressure (psi)
Vs dry (ft/sec)
Vs dry R (ft/sec)
Vs sat (ft/sec)

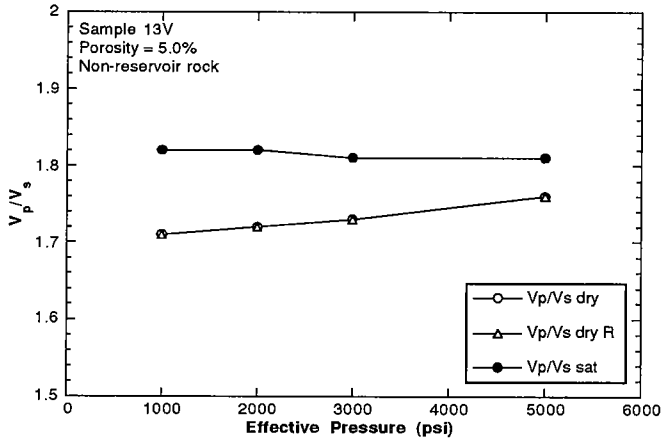
Sample 13V
Porosity = 5.0%
Non-reservoir rock
Vp/Vs
Effective Pressure (psi)
Vp/Vs dry
Vp/Vs dry R
Vp/Vs sat

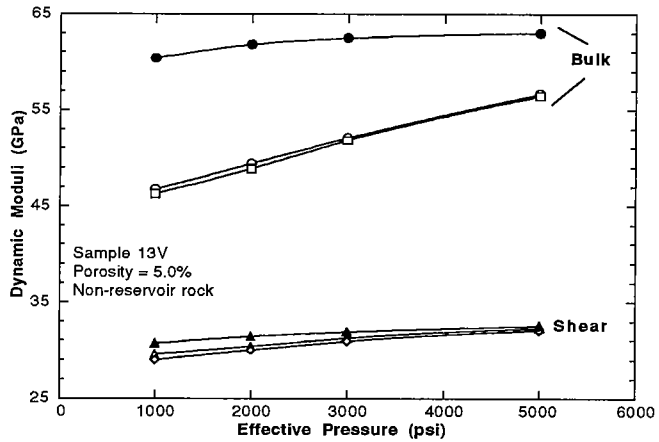
Sample 13V
Porosity = 5.0%
Non-reservoir rock
Dynamic Moduli (GPa)
Effective Pressure (psi)
Bulk
Shear

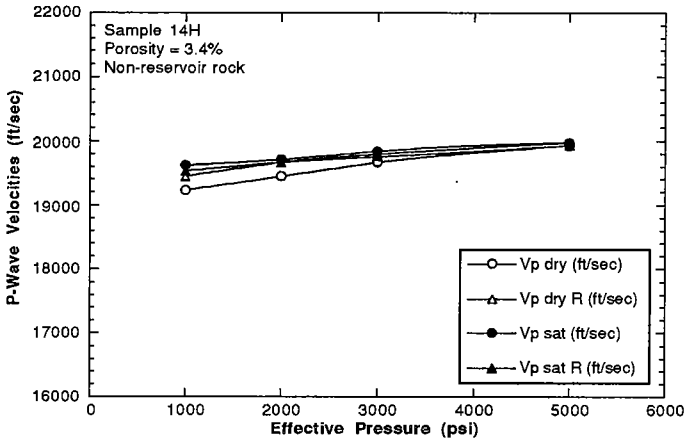
Sample 14H
Porosity = 3.4%
Non-reservoir rock
P-Wave Velocities (ft/sec)
Effective Pressure (psi)
Vp dry (ft/sec)
Vp dry R (ft/sec)
Vp sat (ft/sec)
Vp sat R (ft/sec)

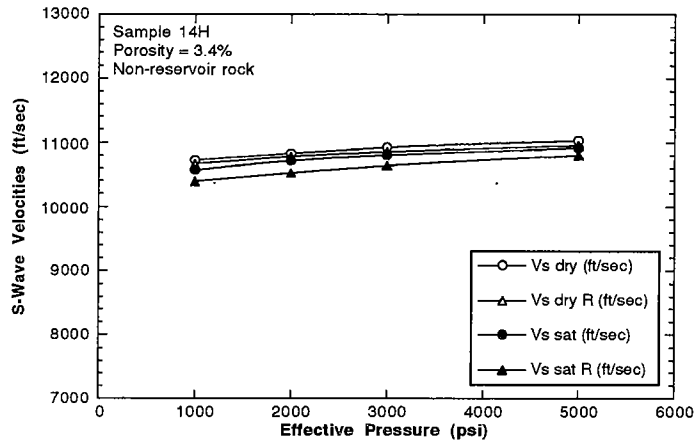
Sample 14H
Porosity = 3.4%
Non-reservoir rock
S-Wave Velocities (ft/sec)
Effective Pressure (psi)
Vs dry (ft/sec)
Vs dry R (ft/sec)
Vs sat (ft/sec)
Vs sat R (ft/sec)

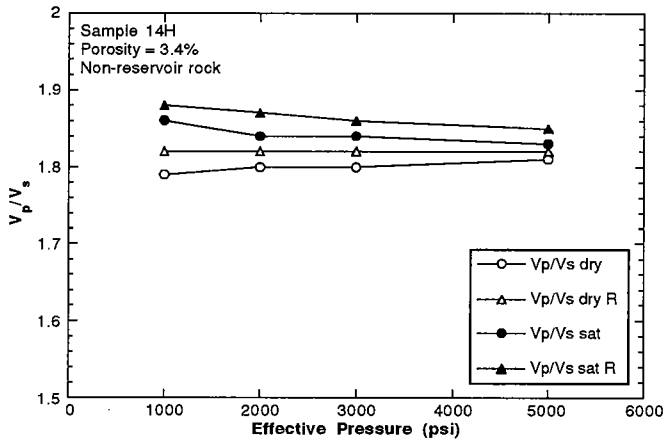
Sample 14H
Porosity = 3.4%
Non-reservoir rock
Vp/Vs
Effective Pressure (psi)
Vp/Vs dry
Vp/Vs dry R
Vp/Vs sat
Vp/Vs sat R

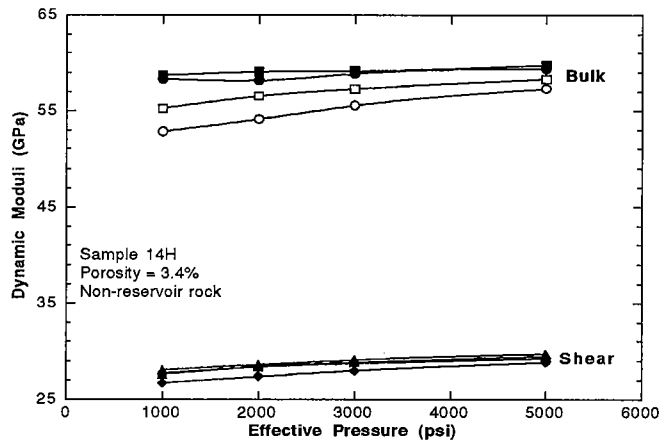
Sample 14H
Porosity = 3.4%
Non-reservoir rock
Dynamic Moduli (GPa)
Effective Pressure (psi)
Bulk
Shear

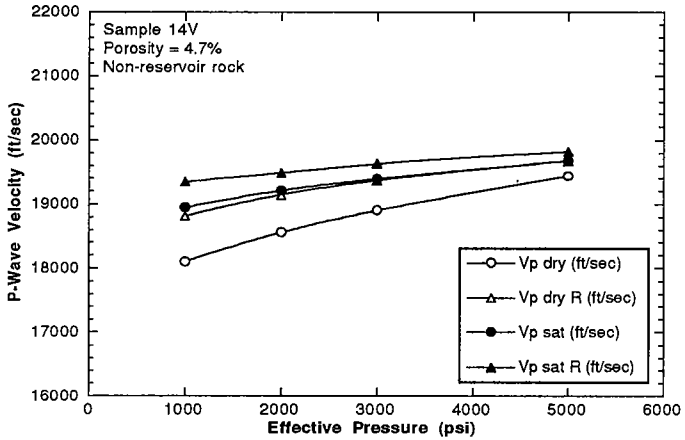
Sample 14V
Porosity = 4.7%
Non-reservoir rock
P-Wave Velocity (ft/sec)
Effective Pressure (psi)
Vp dry (ft/sec)
Vp dry R (ft/sec)
Vp sat (ft/sec)
Vp sat R (ft/sec)

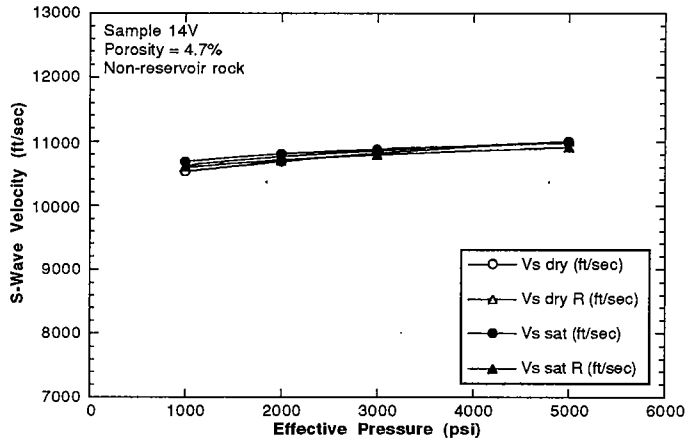
Sample 14V
Porosity = 4.7%
Non-reservoir rock
S-Wave Velocity (ft/sec)
Effective Pressure (psi)
Vs dry (ft/sec)
Vs dry R (ft/sec)
Vs sat (ft/sec)
Vs sat R (ft/sec)

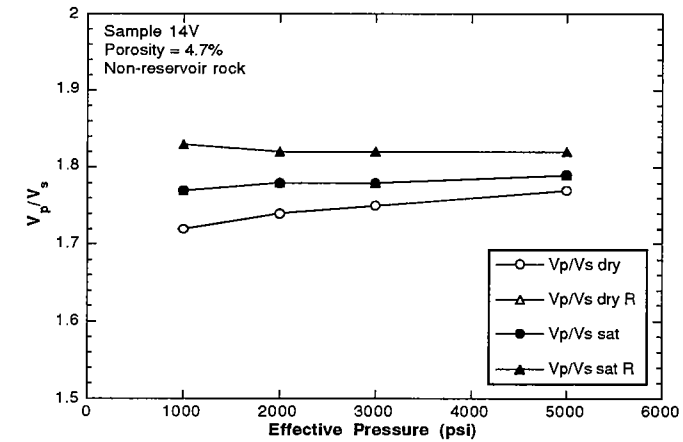
Sample 14V
Porosity = 4.7%
Non-reservoir rock
Vp/Vs
Effective Pressure (psi)
Vp/Vs dry
Vp/Vs dry R
Vp/Vs sat
Vp/Vs sat R

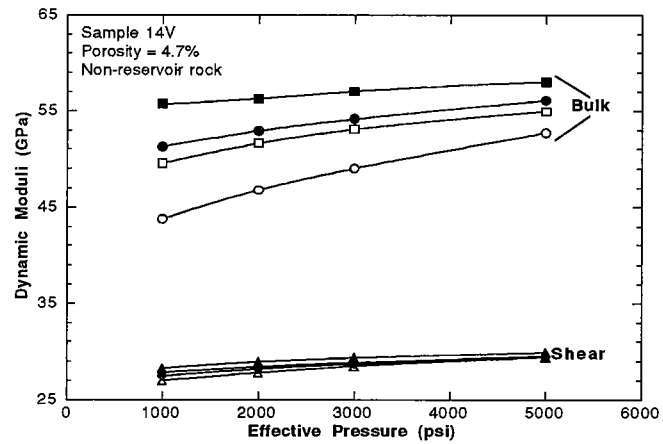
Sample 14V
Porosity = 4.7%
Non-reservoir rock
Dynamic Moduli (GPa)
Effective Pressure (psi)
Bulk
Shear

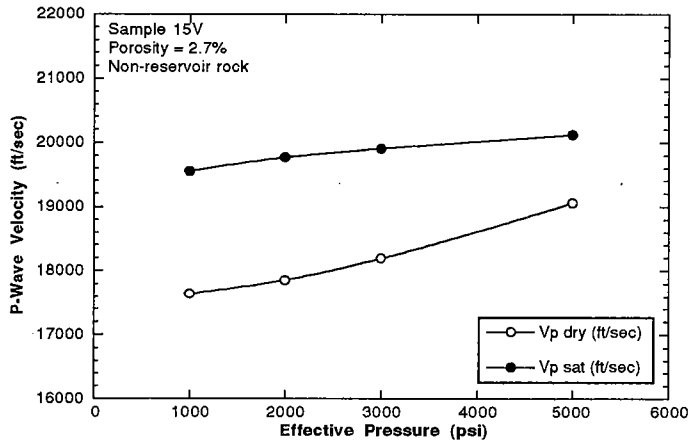
Sample 15V
Porosity = 2.7%
Non-reservoir rock
P-Wave Velocity (ft/sec)
Effective Pressure (psi)
Vp dry (ft/sec)
Vp sat (ft/sec)

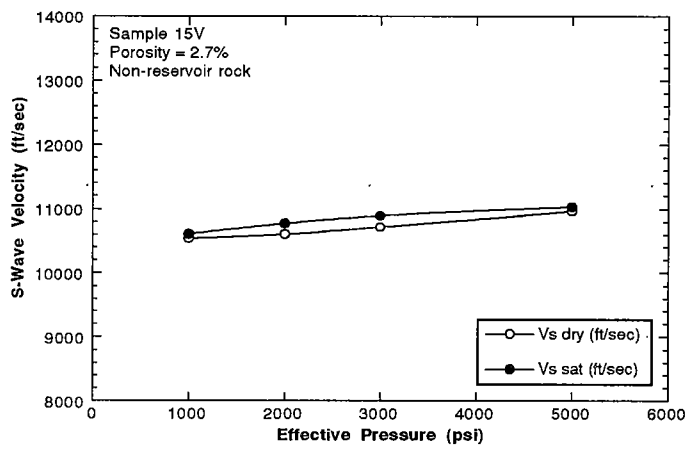
Sample 15V
Porosity = 2.7%
Non-reservoir rock
S-Wave Velocity (ft/sec)
Effective Pressure (psi)
Vs dry (ft/sec)
Vs sat (ft/sec)

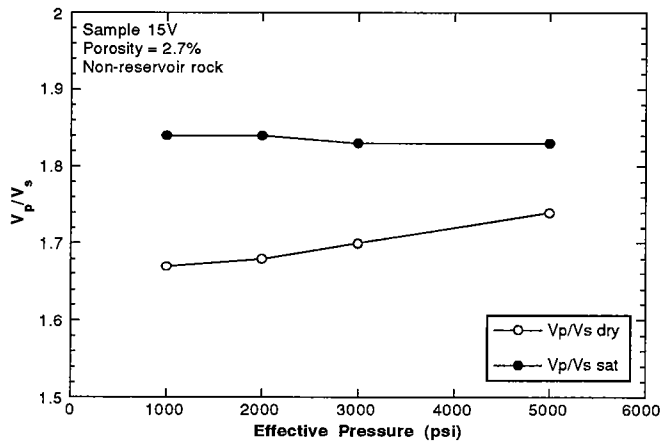
Sample 15V
Porosity = 2.7%
Non-reservoir rock
Vp/Vs
Effective Pressure (psi)
Vp/Vs dry
Vp/Vs sat

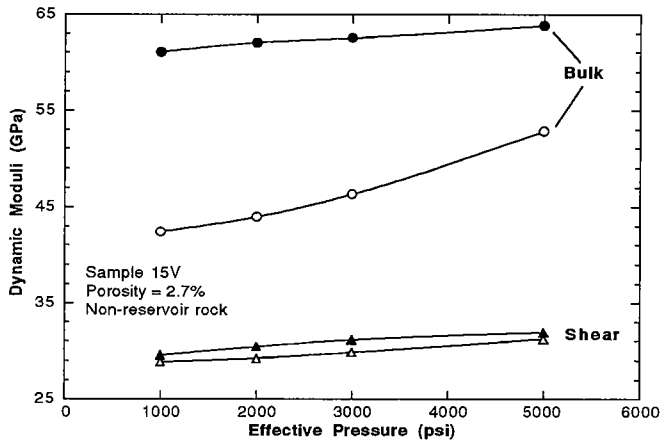
Sample 15V
Porosity = 2.7%
Non-reservoir rock
Dynamic Moduli (GPa)
Effective Pressure (psi)
Bulk
Shear

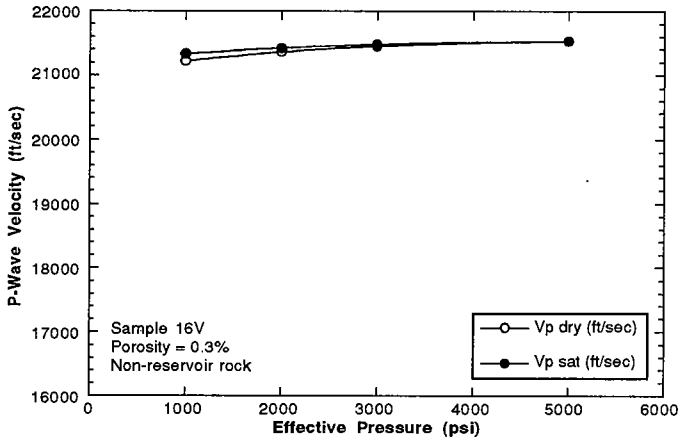
P-Wave Velocity (ft/sec)
22000
21000
20000
19000
18000
17000
16000
0
1000
2000
3000
4000
5000
6000
Effective Pressure (psi)
Sample 16V
Porosity = 0.3%
Non-reservoir rock
Vp dry (ft/sec)
Vp sat (ft/sec)

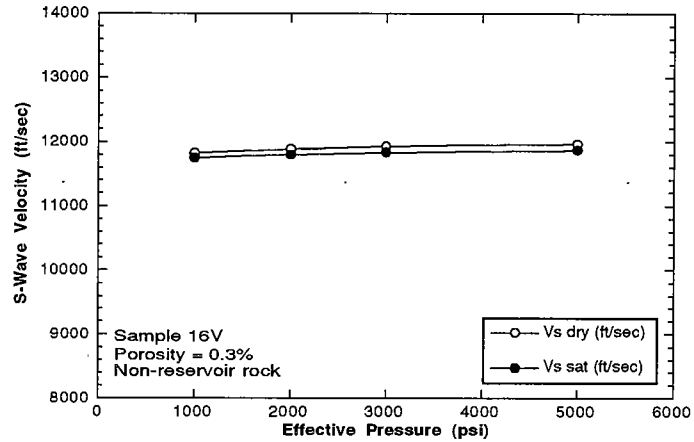
S-Wave Velocity (ft/sec)
14000
13000
12000
11000
10000
9000
8000
0
1000
2000
3000
4000
5000
6000
Effective Pressure (psi)
Sample 16V
Porosity = 0.3%
Non-reservoir rock
Vs dry (ft/sec)
Vs sat (ft/sec)

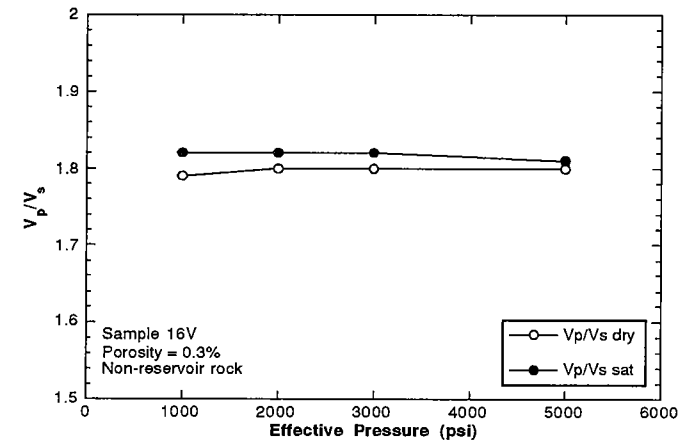
V_p/V_s
2
1.9
1.8
1.7
1.6
1.5
0
1000
2000
3000
4000
5000
6000
Effective Pressure (psi)
Sample 16V
Porosity = 0.3%
Non-reservoir rock
Vp/Vs dry
Vp/Vs sat

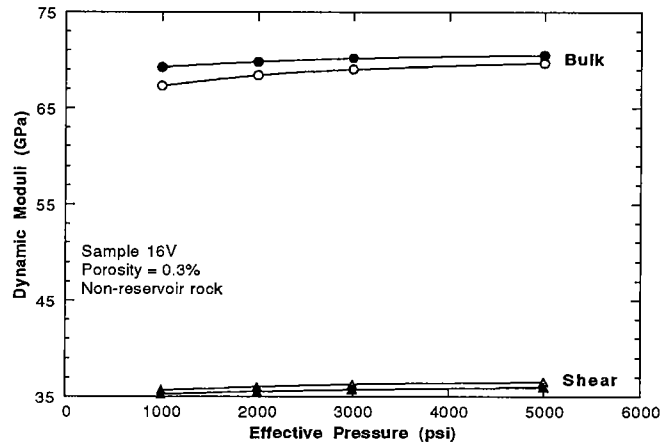
Dynamic Moduli (GPa)
75
65
55
45
35
0
1000
2000
3000
4000
5000
6000
Effective Pressure (psi)
Bulk
Shear
Sample 16V
Porosity = 0.3%
Non-reservoir rock

Appendix B

DOLOMITE-CALCITE TRANSFORM

If we assume the principal minerals of the Grayburg formation are dolomite and calcite, we can estimate the mineral moduli (K_m and G_m) using the following relations:

$$K_m = K_{Clct} + \frac{(K_{Dlmt} - K_{Clct})}{(\rho_{Dlmt} - \rho_{Clct})}(\rho_g - \rho_{Clct}) = 76.7 + 113.125(\rho_g - 2.71) \qquad \text{(B1)}$$

$$G_m = G_{Clct} + \frac{(G_{Dlmt} - G_{Clct})}{(\rho_{Dlmt} - \rho_{Clct})}(\rho_g - \rho_{Clct}) = 32.3 + 83.75(\rho_g - 2.71) \qquad \text{(B2)}$$

where ρ_g is the measured grain density of the sample, K_{Clct} = 76.7 GPa is the bulk modulus of calcite, K_{Dlmt} = 94.8 GPa is the bulk modulus of dolomite, G_{Clct} = 32.3 GPa is the shear modulus of calcite, G_{Dlmt} = 45.7 GPa is the shear modulus of dolomite, ρ_{Clct} = 2.71 g/cm^3 is the grain (mineral) density of calcite, and ρ_{Dlmt} = 2.87 g/cm^3 is the grain density of dolomite. Accordingly, the grain density (ρ_g) is:

$$\begin{aligned} \rho_g(g/cm^3) &= \rho_{Dlmt} + (\partial\rho_g/\partial X_{Clct})X_{Clct} \\ &= 2.87 - 0.16X_{Clct} \end{aligned} \qquad \text{(B3)}$$

where the grain-volume fraction of calcite (X_{Clct}) is:

$$X_{Clct} = \frac{\rho_g - \rho_{Dlmt}}{\rho_{Clct} - \rho_{Dlmt}} = \frac{\rho_g - 2.87}{2.71 - 2.87} \qquad \text{(B4)}$$

and

$$X_{Dlmt} + X_{Clct} = 1. \qquad \text{(B5)}$$

If mineral composition and porosity (ϕ) were the primary factors controlling the dry-frame moduli (K_d and G_d) of these rocks, then these frame moduli are:

$$\begin{aligned} K_d(\text{GPa}) &= K_m + (\partial K_d/\partial\phi)\phi \\ &= K_{Dlmt} + (\partial K_m/\partial X_{Clct})X_{Clct} + (\partial K_d/\partial\phi)\phi \\ &\approx 94.8 - 18.1X_{Clct} + (\partial K_d/\partial\phi)\phi \end{aligned} \tag{B6}$$

and

$$\begin{aligned} G_d(\text{GPa}) &= G_m + (\partial G_d/\partial\phi)\phi \\ &= G_{Dlmt} + (\partial G_m/\partial X_{Clct})X_{Clct} + (\partial G_d/\partial\phi)\phi. \\ &\approx 45.7 - 13.4X_{Clct} + (\partial G_d/\partial\phi)\phi \end{aligned} \tag{B7}$$

When $X_{Clct} = 0$, then $K_m = K_{Dlmt}$ and $G_m = G_{Dlmt}$. When $X_{Clct} = 1$, then $K_m = K_{Clct}$ and $G_m = G_{Clct}$.

The $(\partial K_d/\partial\phi)$ and $(\partial G_d/\partial\phi)$ coefficients are presumed constant and estimated using $-(K_{Dlmt}/\phi_0)$ and $-(G_{Dlmt}/\phi_0)$ so when ϕ approaches from below the "initial" or "depositional" porosity ϕ_0 the dry moduli of a pure dolomite frame are zero. In reality however, these coefficients depend on pore shape and frame architecture.

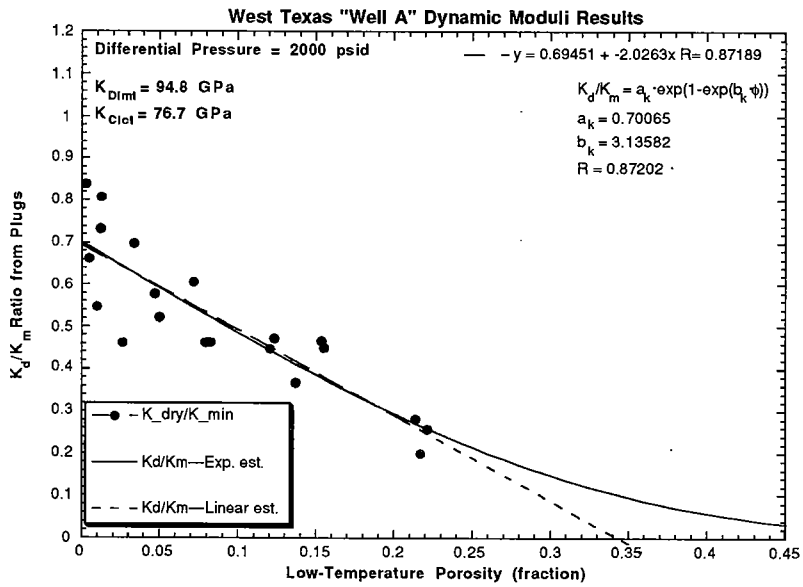

Figure B1

Figure B1: Plot of K_d/K_m vs. low-temperature porosity. Dolomite-calcite transform.

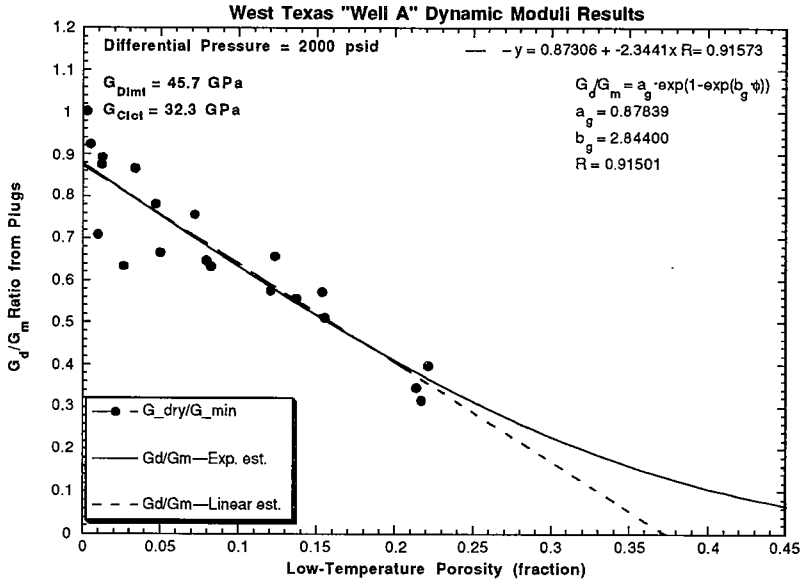

Figure B2

Figure B2: Plot of G_d/G_m vs. low-temperature porosity. Dolomite-calcite transform.

Figures B1 and B2 are plots of K_d/K_m and G_d/G_m, respectively. These plots were generated from the plug data using equations (B1) and (B2) for K_m and G_m, and K_d and G_d calculated from the dry velocity measurements (Table 3). Using the linear least-squares lines from these plots, the frame moduli are:

$$\begin{aligned} K_d(\text{GPa}) &= K_m(\alpha_k - \beta_k\phi) \\ &\approx K_m(0.695 - 2.03\phi) \qquad \ldots \phi_0 = 0.343 \\ &\approx 65.8 - 12.6X_{Clct} - 192.1\phi \end{aligned} \tag{B8}$$

where $\alpha_k = (K_d/K_m)_{\phi=0}$ and $\beta_k = -(\partial K_d/\partial\phi)/K_m = \alpha_k/\phi_0$, and

$$\begin{aligned} G_d(\text{GPa}) &= G_m(\alpha_g - \beta_g\phi) \\ &\approx G_m(0.873 - 2.34\phi) \qquad \ldots \phi_0 = 0.372 \\ &\approx 39.9 - 11.7X_{Clct} - 107.1\phi \end{aligned} \tag{B9}$$

where $\alpha_g = (G_d/G_m)_{\phi=0}$ and $\beta_g = -(\partial G_d/\partial\phi)/G_m = \alpha_g/\phi_0$. These coefficients are lower than the expected theoretical coefficients (i.e., $\alpha_k = \alpha_g = 1$ and $\beta_k = \beta_g = 1/\phi_0$) if

mineral composition (the X_i's) and porosity (ϕ) are the only factors controlling the dry-frame moduli (K_d and G_d) of these rocks. This suggests that the estimates of mineral fractions for the plug samples do not reflect the actual mineralogy. In fact, this dolomite-calcite technique does not reflect the anhydrite, gypsum and quartz contents of these rocks [Harris et al., 1984].

When I used this dolomite-calcite method to generate low-frequency estimates of the saturated-rock velocities to compare to the sonic logs (Figure 11), I found the estimates were generally high.

The exponential curves in Figures B1 and B2 have the form:

$$M_d(\text{GPa}) = M_m \cdot a_j \cdot \exp\left[1 - \exp\left(b_j \cdot \phi\right)\right] \tag{B10}$$

where M_d is the dry modulus (K_d or G_d), M_m is the mineral modulus (K_m or G_m), subscript "j" refers to subscripts "k" or "g" for the K_d and G_d curves in Figures B1 and B2, $a_j = M_d/M_m$, and $b_j = 1/\phi^*$ is the exponent scale factor. When $\phi \rightarrow 0$, then $M_d \rightarrow M_m \cdot a_j$. When $\phi \rightarrow 1$, then $M_d \rightarrow 0$. When $\phi = \phi^* = 1/b_j$, then $M_d = 0.179 \cdot M_m \cdot a_j$.

DOLOSTONE-LIMESTONE TRANSFORM

I explored the possibility that a dolomite-calcite framework was not adequate. If this was true, then we should expect closer agreement between theory and measurement with a different framework composition. If we assume the Grayburg formation is a mix of dolostone and limestone, we can estimate the mineral moduli (K_m and G_m) using the following relations:

$$K_m = K_{Lmst} + \frac{\left(K_{Dlst} - K_{Lmst}\right)}{\left(\rho_{Dlst} - \rho_{Lmst}\right)}\left(\rho_g - \rho_{Lmst}\right) = 72.4 + 43.125\left(\rho_g - 2.71\right) \tag{B11}$$

$$G_m = G_{Lmst} + \frac{\left(G_{Dlst} - G_{Lmst}\right)}{\left(\rho_{Dlst} - \rho_{Lmst}\right)}\left(\rho_g - \rho_{Lmst}\right) = 32.6 + 56.875\left(\rho_g - 2.71\right) \tag{B12}$$

where K_{Lmst} = 72.4 GPa is the bulk modulus of limestone, K_{Dlst} = 79.3 GPa is the bulk modulus of dolostone, G_{Lmst} = 32.6 GPa is the shear modulus of limestone, G_{Dlst} = 41.7 GPa is the shear modulus of dolostone, ρ_{Lmst} = 2.71 g/cm^3 is the grain density of

limestone, and $\rho_{Dlst} = 2.87$ g/cm^3 is the grain density of dolostone. Accordingly, the grain density (ρ_g) is:

$$\begin{aligned}\rho_g(g/cm^3) &= \rho_{Dlst} + \left(\partial\rho_g/\partial X_{Lmst}\right)X_{Lmst} \\ &= 2.87 - 0.16X_{Lmst}\end{aligned} \tag{B13}$$

where the grain-volume fraction of calcite (X_{Lmst}) is:

$$X_{Lmst} = \frac{\rho_g - \rho_{Dlst}}{\rho_{Lmst} - \rho_{Dlst}} = \frac{\rho_g - 2.87}{2.71 - 2.87} \tag{B14}$$

and

$$X_{Dlst} + X_{Lmst} = 1. \tag{B15}$$

Equations (B13) and (B14) produce the same results as (B3) and (B4). This is because we have not changed the grain densities of the pure end-members.

Again, if mineral composition and porosity (ϕ) were the primary factors controlling the dry-frame moduli (K_d and G_d) of these rocks, then these frame moduli are:

$$\begin{aligned}K_d(GPa) &= K_m + \left(\partial K_d/\partial\phi\right)\phi \\ &\approx K_{Dlst} + \left(\partial K_m/\partial X_{Lmst}\right)X_{Lmst} + \left(\partial K_d/\partial\phi\right)\phi \\ &\approx 79.3 - 6.9X_{Lmst} + \left(\partial K_d/\partial\phi\right)\phi\end{aligned} \tag{B16}$$

and

$$\begin{aligned}G_d(GPa) &= G_m + \left(\partial G_d/\partial\phi\right)\phi \\ &\approx G_{Dlst} + \left(\partial G_m/\partial X_{Lmst}\right)X_{Lmst} + \left(\partial G_d/\partial\phi\right)\phi. \\ &\approx 41.7 - 9.1X_{Lmst} + \left(\partial G_d/\partial\phi\right)\phi\end{aligned} \tag{B17}$$

As for the dolomite-calcite estimate, the $(\partial K_d/\partial\phi)$ and $(\partial G_d/\partial\phi)$ coefficients were estimated so when ϕ approaches from below the "initial" or "depositional" porosity ϕ_0 the dry moduli of a pure dolostone frame are zero.

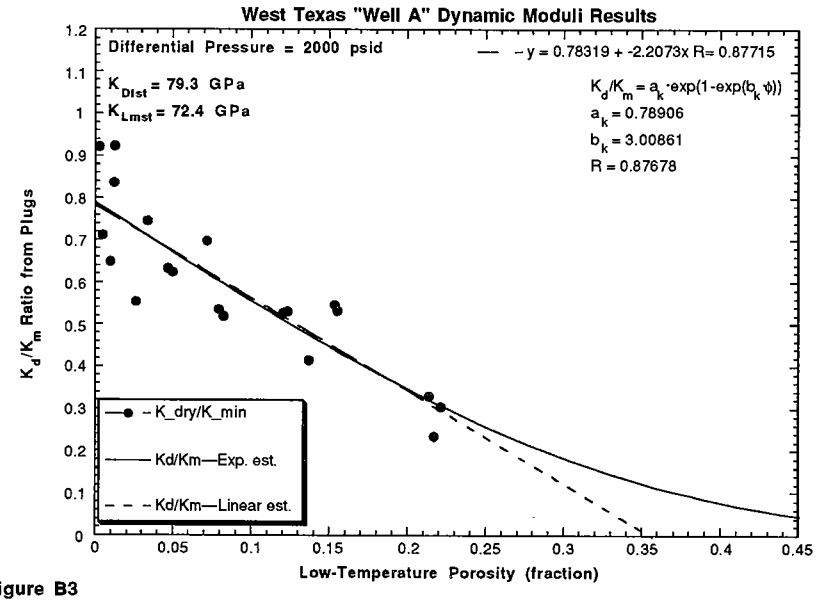

Figure B3

Figure B3: Plot of K_d/K_m vs. low-temperature porosity. Dolostone-limestone transform.

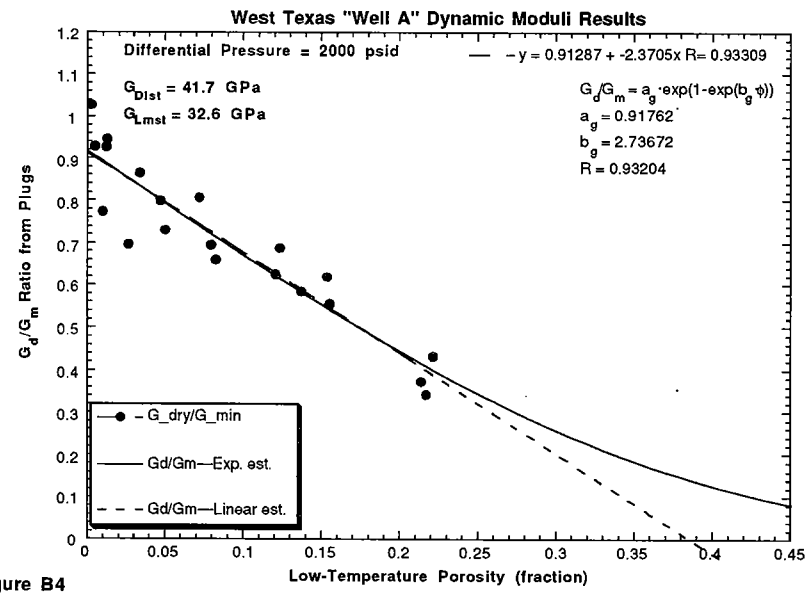

Figure B4

Figure B4: Plot of G_d/G_m vs. low-temperature porosity. Dolostone-limestone transform.

Figures B3 and B4 are plots of K_d/K_m and G_d/G_m, respectively. These plots were generated from the plug data using equations (B11) and (B12) for K_m and G_m, and K_d and G_d calculated from the dry velocity measurements (Table 3). Using the linear least-squares lines from these plots, the frame moduli are:

$$\begin{aligned} K_d(\text{GPa}) &= K_m(\alpha_k - \beta_k\phi) \\ &\approx K_m(0.783 - 2.21\phi) \qquad \ldots \phi_0 = 0.386 \\ &\approx 62.1 - 5.4X_{Lmst} - 160.8\phi \end{aligned} \tag{B18}$$

and

$$\begin{aligned} G_d(\text{GPa}) &= G_m(\alpha_g - \beta_g\phi) \\ &\approx G_m(0.913 - 2.37\phi) \qquad \ldots \phi_0 = 0.385 \\ &\approx 38.1 - 8.3X_{Lmst} - 98.8\phi \end{aligned} \tag{B19}$$

The coefficients are still lower than the expected theoretical coefficients. However, there is closer agreement than for the dolomite-calcite framework case. The ϕ_0 estimates are essentially identical here. This suggests that these dolostone-limestone estimates of mineral fractions are better than the dolomite-calcite estimates. However, the dolostone-limestone framework still may not reflect the actual mineralogy.

When used to generate velocity estimates to compare to the sonic logs (Figure 12), this method resulted in saturated velocities that were closer than those of the dolomite-calcite method (Figure 11).

CORE CONSTRAINED TRANSFORM

Grain Densities

To try to reflect the mineralogy better, I used the full-diameter core measurements of grain density, porosity, gypsum content, and total gamma-ray count to estimate K_m and G_m. I assumed the dominant mineral was dolomite. I constrained the gypsum grain-volume fraction to the core measurements. The total gamma-ray count helped to estimate the quartz silt content in these rocks [Harris et al., 1984], which I assumed varied from 0 to 50 %GV quartz silt. I could not constrain the calcite and anhydrite grain-volume (GV)

fractions using available core data. To obtain an estimate of the grain-volume fractions of these minerals, I started with an estimate (ρ_{Est}) of the grain-density data using

$$\begin{aligned}\rho_{Est} &= \rho_{Dlmt} + \left(\partial\rho_g/\partial X_{Gyps}\right)X_{Gyps} + \left(\partial\rho_g/\partial X_{Qrtz}\right)X_{Qrtz} \\ &= 2.87 - 0.56X_{Gyps} - 0.22X_{Qrtz}\end{aligned} \tag{B20}$$

where ρ_{Dlmt} is the mineral density of dolomite, X_{Gyps} = gypsum grain-volume fraction, and X_{Qrtz} = grain-volume fraction of quartz silt. Positive deviations ($\rho_g > \rho_{Est}$) from this estimate were assumed to result from anhydrite and negative deviations ($\rho_g < \rho_{Est}$) were assumed to result from calcite. Accordingly, the anhydrite mineral fraction (X_{Anhy}) was estimated using

$$\begin{aligned}X_{Anhy} &= \frac{\rho_g - \rho_{Dlmt} + \left(\rho_{Dlmt} - \rho_{Gyps}\right)X_{Gyps} + \left(\rho_{Dlmt} - \rho_{Qrtz}\right)X_{Qrtz}}{\rho_{Anhy} - \rho_{Dlmt}} \\ &= \frac{\rho_g - 2.87 + 0.56X_{Gyps} + 0.22X_{Qrtz}}{0.09}\end{aligned} \quad \ldots\ \rho_g > \rho_{Est} \tag{B21}$$

and the calcite mineral fraction (X_{Clct}) was estimated using

$$\begin{aligned}X_{Clct} &= \frac{\rho_g - \rho_{Dlmt} + \left(\rho_{Dlmt} - \rho_{Gyps}\right)X_{Gyps} + \left(\rho_{Dlmt} - \rho_{Qrtz}\right)X_{Qrtz}}{\rho_{Clct} - \rho_{Dlmt}} \\ &= \frac{\rho_g - 2.87 + 0.56X_{Gyps} + 0.22X_{Qrtz}}{-0.16}\end{aligned} \quad \ldots\ \rho_g < \rho_{Est}. \tag{B22}$$

Finally the dolomite grain-volume fraction was estimated as

$$X_{Dlmt} = 1 - \left(X_{Clct} + X_{Anhy} + X_{Gyps} + X_{Qrtz}\right). \tag{B23}$$

The grain density is therefore given by

$$\begin{aligned}\rho_g &= \rho_{Dlmt} + \left(\frac{\partial\rho_g}{\partial X_{Clct}}\right)X_{Clct} + \left(\frac{\partial\rho_g}{\partial X_{Anhy}}\right)X_{Anhy} + \left(\frac{\partial\rho_g}{\partial X_{Gyps}}\right)X_{Gyps} + \left(\frac{\partial\rho_g}{\partial X_{Qrtz}}\right)X_{Qrtz} \\ &= 2.87 - 0.16X_{Clct} + 0.09X_{Anhy} - 0.56X_{Gyps} - 0.22X_{Qrtz}\end{aligned} \tag{B24}$$

Grain Moduli

I used Hill's [1952] method to calculate the effective mineral moduli of the rocks from the grain-volume fractions derived from equations (B19) to (B22). Hill's method is:

$$K_m = \frac{1}{2}\left[K_{Voight} + K_{Reuss}\right] = \frac{1}{2}\left[\sum_{i=1}^{M} X_i K_i + \left(\sum_{i=1}^{M} \frac{X_i}{K_i}\right)^{-1}\right] \tag{B25}$$

and

$$G_m = \frac{1}{2}\left[G_{Voight} + G_{Reuss}\right] = \frac{1}{2}\left[\sum_{i=1}^{M} X_i G_i + \left(\sum_{i=1}^{M} \frac{X_i}{G_i}\right)^{-1}\right], \tag{B26}$$

where X_i is the grain-volume fraction of the i-th mineral, K_i and G_i are the mineral bulk and shear moduli of the i-th mineral, and subscripts "Voight" and "Reuss" refer to Voight's [1928] isostrain and Reuss' [1929] isostress averaging techniques.

TABLE B1. Mineral Properties

Mineral	ρ_g (g/cm^3)	K_m (GPa)	G_m (GPa)
Dolomite	2.87	94.8	45.7
Calcite	2.71	76.7	32.3
Anhydrite	2.96	66.5	34.2
Gypsum	2.31	58.0	30.0
Quartz (silt)	2.65	38.0	44.4

Dry-Frame Moduli

To estimate the dry-frame moduli, I used the dry velocity measurements from the 20 plug samples (Table 3). After calculating K_d and G_d, I fit the following relations to these moduli (Figures B5 and B6):

$$\begin{aligned} K_d(\text{GPa}) &= K_m(\alpha_k - \beta_k \phi) \\ &\approx K_m(0.733 - 1.99\phi) \end{aligned} \quad \ldots \phi_0 = 0.368 \tag{B27}$$

and

$$G_d(\text{GPa}) = G_m\left(\alpha_g - \beta_g\phi\right) \quad \ldots \phi_0 = 0.387$$
$$= G_m(0.845 - 2.18\phi) \qquad \text{(B28)}$$

The α and β coefficients are lower than expected if mineral composition (the X_i's) and porosity (ϕ) were the only factors controlling the dry-frame moduli (K_d and G_d) of these rocks. The estimates of $\phi_0 = \alpha/\beta$ differ from one another. This suggests either (1) the estimates of mineral fractions for the plug samples do not reflect the actual mineralogy, (2) the plug sampling was too coarse to capture the full range of mineralogy within the Grayburg formation and for the statistics to reflect expected mineral moduli effects, or (3) factors other than just mineralogy and porosity contribute to the dry-frame moduli.

When used to generate velocity estimates to compare to the sonic logs (Figure 13), this method resulted in a fit comparable to the dolostone-limestone (Figure 12). The two figures differ in the low-velocity zone centered around 2860 feet. This is a high gamma-ray zone and the quartz content may be too low. The dolomite-limestone method (Figure 12) produces an overall better fit to the S-wave sonic data than in Figure 13.

This core-constrained method suffers because I could not estimate the calcite and anhydrite fractions together within the same sample, so the results are somewhat unrealistic. The best way to estimate mineral moduli is to use quantitative mineralogy obtained from petrographic and geochemical analyses (e.g., mineral modal analyses).

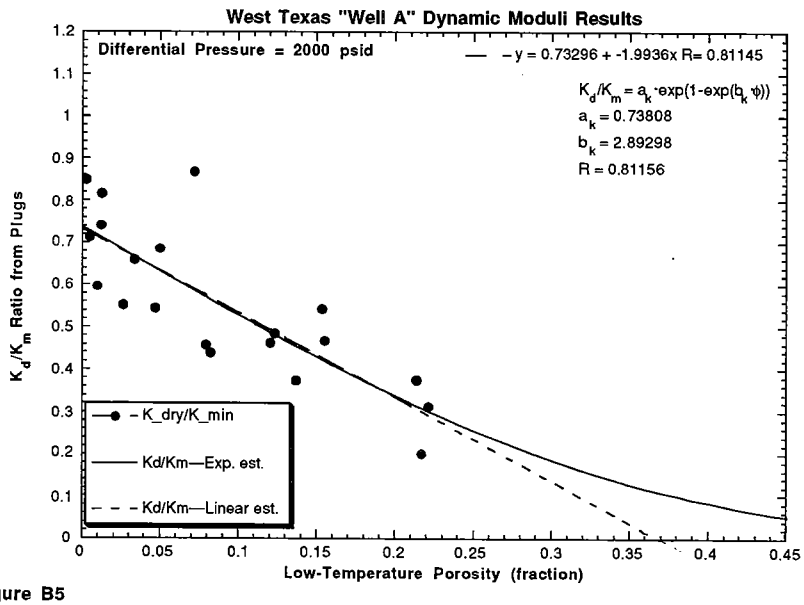

Figure B5: Plot of K_d/K_m vs. low-temperature porosity. Core constrained transform.

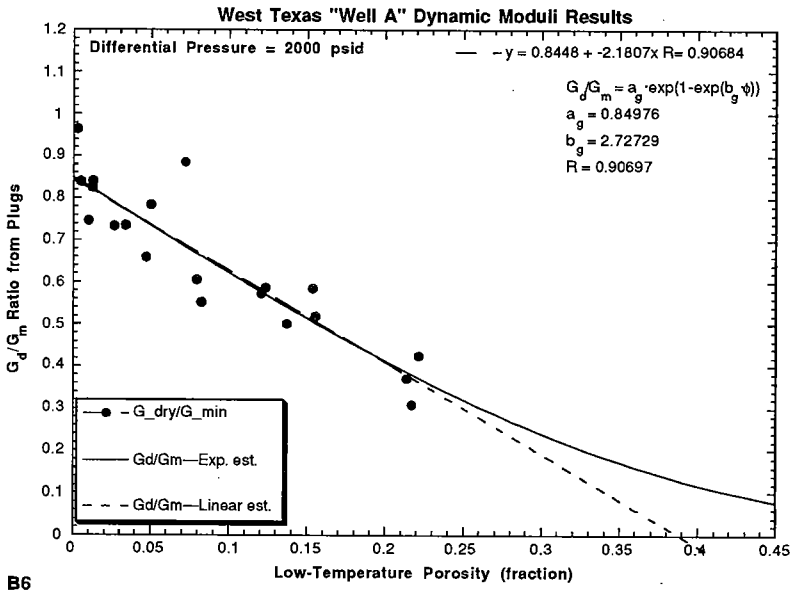

Figure B6

Figure B6: Plot of G_d/G_m vs. low-temperature porosity. Core constrained transform.